

# Runoff required to drive postimpact gully development on the walls of Meteor Crater (Arizona, USA)

Marisa C. Palucis<sup>1,†</sup>, Alan D. Howard<sup>2</sup>, David A. Kring<sup>3</sup>, Kuni Nishiizumi<sup>4</sup>, Marc Caffee<sup>5</sup>, and William E. Dietrich<sup>6</sup>

<sup>1</sup>Department of Earth Science, Dartmouth College, Hanover, New Hampshire 03755, USA

### **ABSTRACT**

Since the impact ~50,000 yr ago, surface runoff has entrained and transported sediment from the walls to the floor of Meteor Crater (Arizona, USA). Previous work interpreted this erosion and deposition to be due to predominantly fluvial (i.e., dilute water transport) processes. However, light detection and ranging (LiDAR)-derived topographic data and field observations indicate that debris flows dominated, which were likely generated by runoff that entrained the talus that borders bedrock cliffs high on the crater walls. The low gradient of the crater floor caused debris flows to stop, leaving lobate deposits, while fluvial processes delivered sediment toward the center of the crater. Cosmogenic radionuclide dating of levee deposits suggests that debris-flow activity ceased in the late Pleistocene, synchronous with regional drying. Assuming a rock-to-water ratio of 0.3 at the time of transport by mass flows, it would have taken  $\sim 2 \times 10^6$  m<sup>3</sup> of water to transport the estimated  $\sim 6.8 \times 10^6$  m<sup>3</sup> of debris-flow deposits found at the surface of the crater floor. This extensive erosion would require ~6 m of total runoff over the 0.35 km<sup>2</sup> upslope source area of the crater, or ~18 mm of runoff per debris-flow event. Much more runoff did occur, as evidenced by crater lake deposits, Holocene fluvial activity (which produced little erosion), and contemporary rainfall rates. Rarely on Earth is the total amount of water that creates and runs through a landscape estimated, yet such calculations are commonly done on Mars. Our analysis suggests that

Marisa C. Palucis **b** https://orcid.org/0000-0003-0034-5810

†marisa.c.palucis@dartmouth.edu

erosional and depositional landforms may record only a small fraction of the total runoff.

### INTRODUCTION

Meteor Crater, a well-preserved impact crater located on the Colorado Plateau in north-central Arizona (35°1.648′N, 111°1.363′E; Fig. 1A), formed  $\sim$ 49,000–61,000 yr ago (Sutton, 1985; Phillips et al., 1991; Nishiizumi et al., 1991; Marrero et al., 2010; Barrows et al., 2019) during the Pleistocene, when climatic conditions were generally cooler and wetter (compared to present day) across the southwestern United States (e.g., Ballenger et al., 2011; Cole et al., 2013). Since Meteor Crater's formation, a network of gullies has developed along its inner walls (Figs. 1B and 1C), which were first discussed in detail by Kumar et al. (2010). Similar features on Mars have gained considerable attention since being recognized by Malin and Edgett (2000), who identified three main attributes to these landforms: a gully head or alcove, channels or chutes, and a fan or apron (Fig. 2). As gullies have been hypothesized by some to have formed from liquid water or brines (Malin and Edgett, 2000; Hartmann et al., 2003; Coleman et al., 2009; see review by Conway et al., 2019), versus dry or gas-supported flows, and have been mapped across geologically young terrains on Mars when liquid water was thought to be highly unstable (Late Amazonian; Harrison et al., 2015), constraining their formation mechanism has been a key goal for understanding recent Martian climate and water reservoirs.

However, the water sources and volumes required to form Martian gullies and erode crater walls through time are uncertain. Models used to assess water amounts on Mars are typically derived from field studies on Earth (e.g., Costard et al., 2002, 2007; Hartmann et al., 2003;

Conway et al., 2015, 2018, 2019), but field studies on Earth rarely ask the question: How much water did it take to make and modify this landscape? Additionally, one important aspect that does not appear to have been considered in previous terrestrial gully studies is the effect of a drying climate on their evolution. This is especially important on Mars, where current conditions are cold and dry, but gully formation may have initiated during periods of high obliquity (Laskar et al., 2004), when there was enhanced potential for precipitation and runoff of water at lower latitudes. Meteor Crater, as first pointed out by Kumar et al. (2010), provides an opportunity to explore how a landscape relevant to Mars with a known initial condition (i.e., a fresh impact crater) has evolved over a geologically short period of time but under significant climate change. Careful mapping of its deposits, using both sedimentology and their surface expression, allows researchers to assess the dominant flow processes (i.e., fluvial vs. debris flow), which is necessary to model the water fluxes and volumes required to form gullies. Furthermore, using a combination of radiometric dating and the fact that there is near-complete conservation of sediment mass in the crater, it is possible to infer changes in the frequency and intensity of runoff events that drove crater evolution.

Observations at Meteor Crater made by Kumar et al. (2010) led them to propose a time sequence of events for the formation and modification of the gullies at Meteor Crater. Immediately postimpact, crater-wall collapse preferentially occurred along the concentric fracture network (mapped by Kumar and Kring, 2008), forming the larger gullies exposed on the crater's corners. A lake then formed at the bottom of the crater, where 30 m of lake sediments cover allogenic breccias with no intervening alluvium (Shoemaker and Kieffer,

*GSA Bulletin*; March/April 2024; v. 136; no. 3/4; p. 1003–1022; https://doi.org/10.1130/B36863.1. Published online 12 July 2023

<sup>&</sup>lt;sup>2</sup>Planetary Science Institute, Tucson, Arizona 85719, USA

<sup>&</sup>lt;sup>3</sup>Lunar and Planetary Institute, Houston, Texas 77058, USA

<sup>&</sup>lt;sup>4</sup>Space Sciences Laboratory, University of California, Berkeley, Berkeley, California 94720, USA

<sup>&</sup>lt;sup>5</sup>PRIME Lab, Department of Physics, Purdue University, West Lafayette, Indiana 47907, USA

<sup>&</sup>lt;sup>6</sup>Department of Earth and Planetary Science, University of California, Berkeley, Berkeley, California 94720, USA







Figure 1. (A) Location of Meteor Crater, Arizona (USA), marked with a yellow star. The location of the Winslow airport, which is 42 km from Meteor Crater, and other relevant locations discussed herein are marked with black dots. Box outlines the Black Mesa study region of Zhu et al. (1998) and Zhu and Kipfer (2010). (B) Image of Meteor Crater (credit: William E. Dietrich, University of California, Berkeley). The crater is ~180 m deep and 1.2 km in diameter with a rim crest that rises ~30 m to 60 m above its surrounding plains. (C) Image of the northeastern wall, which is ~180 m tall, highlighting the main components of a Meteor Crater gully system, which consists of the upper bedrock wall, where runoff is generated during precipitation events, a gully head that is incised into talus/breccia that mantles the crater walls, a gully channel, and a depositional zone (which often consists of coarse-grained lobate-shaped deposits). Latitude, longitude = 35.0278°N, 111.0222°W.

1979). Since the crater is not breached, Kumar et al. (2010) assumed that the source of water for the lake was artesian flooding, groundwater springs, rainfall, or some combination of the three. Surface runoff initially washed craterwall impact deposits into the lake and then later incised bedrock. Kumar et al. (2010) proposed that lake-level fluctuations would result from varying groundwater seepage exfiltrating from radial fractures and tear faults. These proposed seepage outflow channels would then erode the crater walls and deposit sediment across the lower slopes and crater floor (i.e., the Pleistocene alluvium mapped by Shoemaker and Kieffer, 1979) and interfinger with lake sediments. To explain gullies in the lower slopes of the crater wall, Kumar et al. (2010) proposed that a later, second phase of enhanced precipitation occurred, where material deposited from this post-Pleistocene gully-forming event is now being dissected and overlapped, on the crater

floor, with modern playa deposits. They suggested that current-day processes are limited to modification of the gullies by a few debris-flow events, as evidenced by "rock channels with rock levees" on the lower slopes of the crater walls (Kumar et al., 2010, 616). No grainsize data, channel slopes, channel geometry, or other quantitative metrics that might support the inference that fluvial processes are the dominant erosive and transporting agent were reported by Kumar et al. (2010).

Our initial visit to Meteor Crater occurred after Kumar et al. (2010) suggested an alternate hypothesis for the processes driving gully formation. The sedimentology and morphology of many of the deposits along the lower walls of the crater, which are dominated by matrix-supported levees and lobate snouts, indicate that many individual debris-flow events occurred in the past. Furthermore, the weathered state of these deposits suggested a possible Pleistocene, rather

than Holocene, origin. Deposits recording fluvial processes appeared to be subsidiary and more recent. These observations warranted another investigation of the erosional processes (and the resulting deposits) at Meteor Crater, with a specific emphasis on the link between sediment transport process and climate and an assessment of the amount of runoff that would have been necessary to erode the crater-wall gullies.

To obtain a quantitative estimate of the proportion of sediment moved by debris-flow processes, as compared to fluvial processes, we acquired aerial light detection and ranging (LiDAR) data for the crater ( $\sim$ 0.25 m per pixel; point density = 5.4 points/m²), performed detailed field mapping and surveying of the debris-flow levee deposits, collected samples for cosmogenic  $^{10}Be$  dating of several deposits exiting one of the gully systems, and calculated the erosional flux and minimum water runoff associated with sediment deliv-

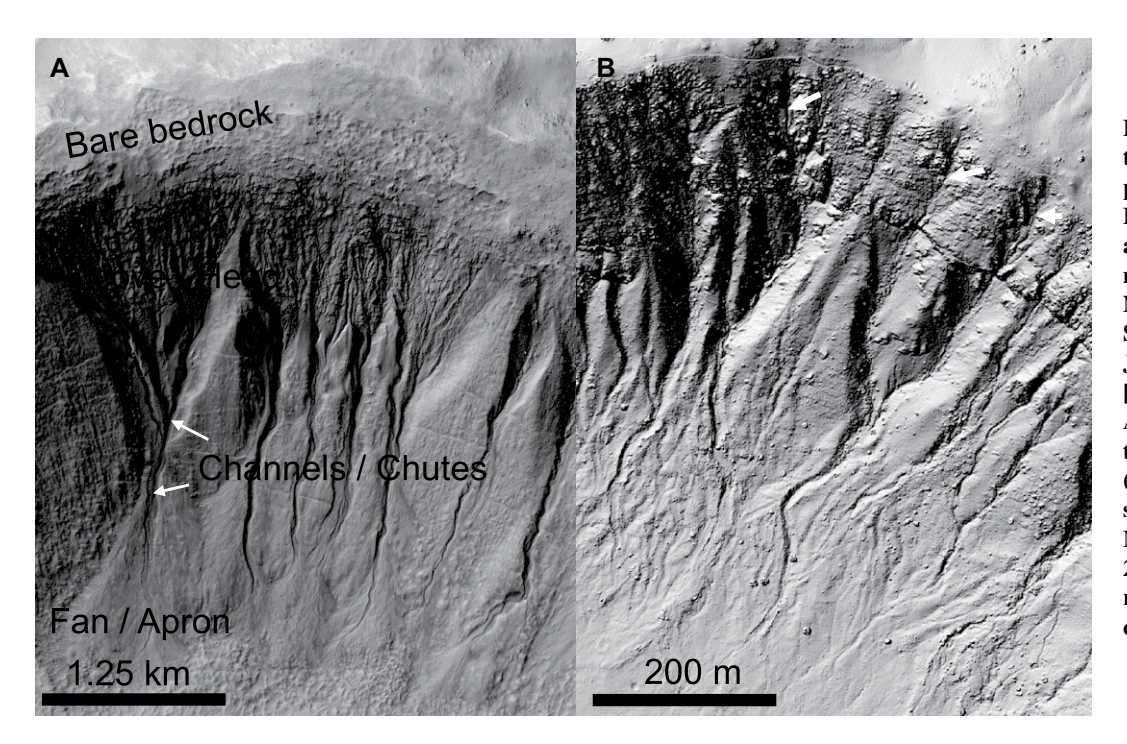


Figure 2. (A) High Resolution Imaging Science Experiment (HiRISE) image ESP\_050858\_1435 of gullies in a small crater in the Terra Cimmeria region of Mars (credit: National Aeronautics Space Administration [NASA]/ Jet Propulsion Laboratory [JPL]-Caltech/University Arizona). Latitude, longitude = 28.0145°N, 261.3920°W. (B) Shaded relief image of the southeastern crater wall of Meteor Crater generated with 25 cm/pixel light detection and ranging (LiDAR) data (https:// opentopography.org/).

ery to the crater floor. Here, we present data that suggest debris-flow processes dominated gully incision up until the Holocene. We then address three central questions: (1) Why did debris flows happen here, and why did they cease? (2) How much water was required to accomplish the observed erosion? (3) Is Meteor Crater an appropriate analog for understanding gullies on Mars? We conclude with a general conceptual model of gully formation processes that we propose is broadly applicable to steep escarpments (on Earth and Mars), where the lower portions are mantled with coarse debris embedded with some finer-grained sediment.

### STUDY SITE

### Geology

Meteor Crater is a simple, bowl-shaped impact crater, ~180 m deep (from the currentday central floor to the crater-rim top) and 1.2 km in diameter (1.1 km<sup>2</sup> in area), and it is encompassed by a rim of ejecta that rises 30-60 m above the surrounding plain (Shoemaker, 1959). Independent dating using <sup>10</sup>Be/<sup>26</sup>Al measurements (Nishiizumi et al., 1991; Barrows et al., 2019), cosmogenic <sup>36</sup>Cl measurements (Phillips et al., 1991; Marrero et al., 2010), and thermoluminescence dating of shock-metamorphosed dolomite and quartz (Sutton, 1985) places the age of the impact between  $\sim$ 49,000 to  $\sim$ 61,000 yr ago, corresponding to the Wisconsin interstadial, which was a relatively warm period (Jacobs,

1985). Shoemaker (1959, 1987), Shoemaker and Kieffer (1979), Kring (1997, 2007, 2017), Kumar and Kring (2008), and Kumar et al. (2010) provided detailed descriptions of the bedrock, ejecta, structure, and surface deposits at Meteor Crater, which are only briefly summarized here. The rocks exposed in the crater range from the Coconino Sandstone (Permian) to the Moenkopi Formation (Triassic), which are units in the upper portion of the Grand Canyon sequence (Dutton, 1882). The lowest exposed unit in the crater is the Coconino Sandstone, composed of well-sorted quartz eolian sands (McKee, 1947). It is the basal unit excavated by the impact event, but only the upper portions of the formation are exposed in the crater walls. The Coconino Sandstone is overlain by  $\sim 1.5$  m of Toroweap Formation, composed of sandstone and dolomite. The Kaibab Formation, an ~80-m-thick unit of dolomite, dolomitic limestone, and thin calcareous sandstone horizons, overlies the Toroweap Formation. The Kaibab Formation is exposed along the steep upper wall of the crater. Shoemaker and Kieffer (1974) mapped the Toroweap Formation as being conformable with the Kaibab Formation, although it is recognized as being distinct in outcrops (and unconformable in other areas of northern Arizona; Kring, 2007). Two members of the Moenkopi Formation rest disconformably on the Kaibab Formation. The bottom member is the Wupatki Member, which is 2-6 m thick and composed of very fine sandstone. Atop the Wupatki Member, there is the Moqui Member,

which is 2-10 m thick and composed of fissile siltstone. The overturned rim sequence occurs in this unit, and because of the fissile nature of the Moqui Member, pinpointing the contact between the upright and overturned Moenkopi strata in the rim is difficult. On average, the exposed Moenkopi Formation is  $\sim 8.5$  m thick (Kring, 2007). The bedrock units in the crater walls are crosscut by faults produced during the impact. Authigenic breccias occur along those faults in near-vertical planes.

Based on the geologic map (Fig. S1<sup>1</sup>) and cross section by Shoemaker (1960), the crater

<sup>&</sup>lt;sup>1</sup>Supplemental Material. Figure S1: Geologic map of Shoemaker (1960) that was recolored by Kring (2007) and has been georeferenced to compare with our geomorphic mapping to highlight the correspondence of the debris-flow levees and snouts with material mapped as Pleistocene alluvium. Figure S2: Highly fractured and broken bedrock wall above gully 0. Figure S3: (A) 0.5 m contours draped over shaded relief image of gully 0 to show our definition of gully head area (blue region) and length (black line), (B) long profiles of the floor of the gully (black line in A) vs. unincised talus/breccia (red line in A), where, on average, gully channels tend to be more concave up than their surrounding unincised talus slopes, and (C) cross section of the gully channel (dashed line in A), highlighting its inner steep walls and U-shape. Figure S4: The location and ID of the individual gully alcoves. Figure S5: (A) Example of a line of individual boulders comprising an older levee at gully 16, and (B) corresponding topographic map, with 0.25 cm contours, showing that the boulders are visible within the LiDAR DEM. Please visit https://doi.org/10.1130/GSAB.S.22362976 to access the supplemental material, and contact editing@ geosociety.org with any questions.

floor is brecciated bedrock (where the bottom of the breccia lens is the boundary between the Coconino Formation and the underlying Supai formation), locally over 150 m thick, covered by  $\sim 10.5$  m of bedrock debris, which is most likely fallout debris from the impact. Atop these postimpact sediments, the crater floor and lower crater walls are covered with Holocene and Pleistocene surficial deposits and breccia. Pleistocene breccia (derived from the impact and fault gouge) borders the lowest portions of the crater walls and is preserved where covered by rockfall derived from erosion of the steep and highly fractured upper crater walls (Fig. S2; Kumar et al., 2010). This talus mantle has been dissected, producing alluvium that interfingers a series of lake beds that are  $\sim$ 30 m thick near the center of the crater. Overlying Pleistocene sediments are ~1.8 m of Holocene alluvium, including the floors of minor stream courses (Shoemaker, 1987), rock levees (Kumar et al., 2010), and playa beds. The uppermost 30 cm of playa bed sediments were deposited above a thin ash layer that was deposited after an eruption from Sunset Crater ∼900 yr ago in the nearby San Francisco volcanic field (Kring, 2007, 2017).

#### **Current and Past Climate**

The current climate at Meteor Crater is hot and arid. The Winslow station, which is located ~30 km east of Meteor Crater, reports annual rainfall of ~200 mm and mean annual snowfall of  $\sim$ 300 mm (https://wrcc.dri.edu/). The wettest month in the region is August, which averages  $\sim$ 35 mm of rain, and the driest month is June with  $\sim$ 5 mm. Over 35% of the yearly precipitation occurs in the fall months, and 15% occurs in the summer months. The maximum daily precipitation on record (over the past 80 yr) was ~99 mm. Based on the regional intensityduration-frequency (IDF) curves (National Oceanic and Atmospheric Administration [NOAA], 2011), 15 to 30 min storm intensities, which are relevant for generating surface runoff and initiating mass flows in the region (Staley et al., 2020), range from  $\sim$ 8–11 mm (1 yr recurrence interval) to  $\sim$ 17–23 mm (decadal recurrence interval) to  $\sim$ 29-40 mm (100 yr recurrence interval) to  $\sim$ 45–60 mm (1000 yr recurrence interval). July tends to be the hottest month, with average highs of  $\sim$ 94 °F (34.4 °C), and January is the coldest, with lows of  $\sim$ 21 °F (-6.1 °C). The groundwater table is below the observable crater floor, which is dry except for minor ponding after rainstorms (Kumar et al., 2010). Roddy (1978) reported that the water level in the Meteor Crater well, located 1050 m north of the point of impact (35°2.188'N, 111°1.399'E), was 186 m below the ground surface (at 1500 m relative to mean

sea level [MSL]), putting the water table  $\sim$ 60 m below the current crater floor. Pilon et al. (1991) used ground-penetrating radar on both the interior floor of the crater (four transects) and across the ejecta (one transect) to locate the water table and found it to be  $\sim$ 65 m below the crater bottom (or 1440 m MSL), in good agreement with the well reading.

However, interpretations of the crater-floor sedimentology suggest that at the time of impact, wetter conditions may have prevailed. Based on the immediate formation of lake deposits postimpact and the presence of a small hill of sediment on the crater floor composed of Pleistocene lake sediments (i.e., Silica Hill), Shoemaker and Kieffer (1979) proposed that at the time of impact, the water table was 30-40 m higher (1536-1546 m MSL) than the current water level. Roddy (1978), however, pointed out that shock compression of the Coconino sandstone could have induced high pore pressures, thereby forcing water to flow upward into the crater, allowing for a lake to form without the crater floor intersecting the local groundwater table. Mollusk populations within the lake core samples indicate perennial waters, as opposed to fluctuating waters (i.e., bogs, swamps, drying muds; Reger and Batchelder, 1971), suggesting that the lake at Meteor Crater was not short-lived and required a sustained source of water.

Although other local paleoclimatic data are lacking, regional studies strongly indicate a late Pleistocene wet period followed by a warming and drying trend toward current conditions. Cole et al. (2013) collected 60 packrat middens across the southwestern United States that ranged from older than 48,000 yr B.P. to present, where well-preserved pine needles within the middens documented the geographic response of three types of pinyon pines to climate change. Their analysis suggested that in northwestern to central Arizona, during the full glacial Wisconsinan (23.4-14.7 ka), winter precipitation was at least 150% greater than current day. During the subsequent Bølling-Allerød interstadial (14.7-13 ka), rapid expansion of these species into central Arizona suggests warmer temperatures than most of the latest Wisconsinan and summer precipitation that was 120% greater than current day. This was followed by rapid warming and precipitation decline at the start of the Holocene (11.7-9.0 ka), which led to the decline and northward retreat of these populations to their current-day distributions (Cole et al., 2013).

To the north of Meteor Crater in the Black Mesa basin in northeastern Arizona (see region in Fig. 1A), Zhu et al. (1998) and Zhu and Kipfer (2010) performed groundwater dating, numerical modeling, and noble gas analyses of the Navajo Sandstone aquifer. They proposed

that 14,000–17,000 yr ago, the recharge rates to groundwater were three times higher relative to today, and the water level was as much as 60 m higher relative to today. They suggested this pulse of high recharge was due to a northward migration of the southern branch of the split jet stream. At the transition to the Holocene, a shift toward the current drier and warmer conditions has been documented in various studies in the region (Cave of Bells area; Fig. 1A; e.g., Wagner et al., 2010), although the specific timing and magnitude of changes vary among studies (e.g., Ballenger et al., 2011).

### METHODOLOGY

### **LiDAR Data Collection and Processing**

On 12 March 2010, the National Center for Airborne Laser Mapping (NCALM) performed an airborne survey of Meteor Crater and its ejecta blanket. To obtain higher-resolution data of the gullies and their meter-scale deposits, two different point densities were used; data at a density of 8 points/m<sup>2</sup> were collected for the crater walls and rim, and data at a density of 4 points/m<sup>2</sup> were collected for the surrounding area. All data processing, including generation of the final data product used in this study, was performed by NCALM. All coordinates are relative to the North American Datum of 1983 (NAD 83; Continually Operating Reference Stations [CORS] 96) reference frame, and no bare earth extraction was required since Meteor Crater is sparsely vegetated, and the bare-earth classification algorithm would smooth out the small-scale topographic features of interest inside of the crater. The elevation and intensity data were interpolated at 25 cm cell sizes using Golden Software's Surfer 8 kriging algorithm. The final product was projected in Universal Transverse Mercator (UTM) zone 12N with units in meters, and heights are North American Vertical Datum of 1988 (NAVD 88) orthometric heights computed from Geodetic Reference System of 1980 (GRS 80) ellipsoid heights using the National Geodetic Survey (NGS) GEOID09 model. The elevation accuracy is 5–30 cm ( $1\sigma$ ). All data can be accessed through the National Science Foundation-supported OpenTopography portal.

#### **Sediment Volume Calculations**

Much of the topographic analysis presented herein (i.e., calculation of the volume of material eroded from talus and levee and lobate deposit volumes) relied on methods like those developed by Warner et al. (2011). To estimate the volume of sediment that has eroded from the talus slopes that border the bedrock cliffs within the crater, we mapped regions of incision and then projected a smooth surface between the bounding sidewalls, essentially recreating the pre-eroded talus slope topography. This projected surface was then gridded and subtracted from the original gridded topography. To estimate the levee and terminal deposit volumes on the surface of the crater floor (i.e., nonburied deposits), we first eliminated the topographic data under the deposit (mapped in planform) and projected the local topography (typically the crater wall or floor) laterally under the deposit to create a predeposit surface. We then took the difference between the gridded current-day deposit surface and the projected predeposit surface to estimate the volume of the deposit. To estimate the volume of sediment deposited on the crater floor as lake sediment, we used the contour at the maximum extent of the lake (at 1570 m [dark blue contour in Fig. 3], the top of "Silica Hill"; Kring, 2007) to estimate its areal extent and multiplied that by the average depth of the lake deposits based on drill cores ( $\sim$ 30 m). To estimate the volume of Holocene alluvium

and playa deposits, we used the geologic map from Shoemaker and Kieffer (1974), which we georeferenced into ArcMap (Fig. S1), to map their areal extents and then multiplied those by 1.8 m, i.e., the depth reported in Shoemaker (1987). To estimate the volume of Pleistocene sediment on the crater floor, we used two methods. The first was to simply map the area these deposits currently occupy on the crater floor and walls (using the geologic map from Shoemaker and Kieffer, 1974) and multiply that by their average depths based on the cross section by Shoemaker and Kieffer (1974). The second method involved fitting second-order polynomials to the boundaries defining the interfaces between the breccia and Pleistocene talus/lake sediment/alluvium and the modern-day crater surface. Shell integration was then used to integrate these functions along the axis perpendicular to the axis of revolution (in this case, we revolved around the y axis and integrated along the x axis). As the "volume" above the breccia had Pleistocene talus, alluvium, and lake sediments, we estimated the percentage of each (Pleistocene talus  $\sim$ 7%, alluvium  $\sim$ 28%, and lake sediment  $\sim$ 65%) from the Shoemaker and

Kieffer (1974) cross section and then applied that to the total volume. These methods inherently assume the crater is a perfect bowl-shape and that deposition of each unit was uniform around the crater; as neither is the case, these are rough estimates of the volumes of each depositional unit.

### **Geomorphic Field Mapping and Surveys**

The relative roles of debris-flow versus fluvial processes at Meteor Crater were determined from examination of surficial deposits and exposures across the crater, and detailed measurements were made in one individual gully system, referred to herein as "gully 0." Criteria used to distinguish past debris-flow events included the presence of boulder-rich lobate snouts, debris-flow tracks (i.e., identified by a single or paired narrow train of boulders or boulders suspended in a fine-grained matrix), poorly sorted and matrix-supported sediments, and the absence of stratification, sorting, or rounding of clasts (e.g., Bull, 1977). Fluvial processes were identified by V-shaped channels with defined banks, sorting and rounding of clasts, clast imbrication, and the development of bed or

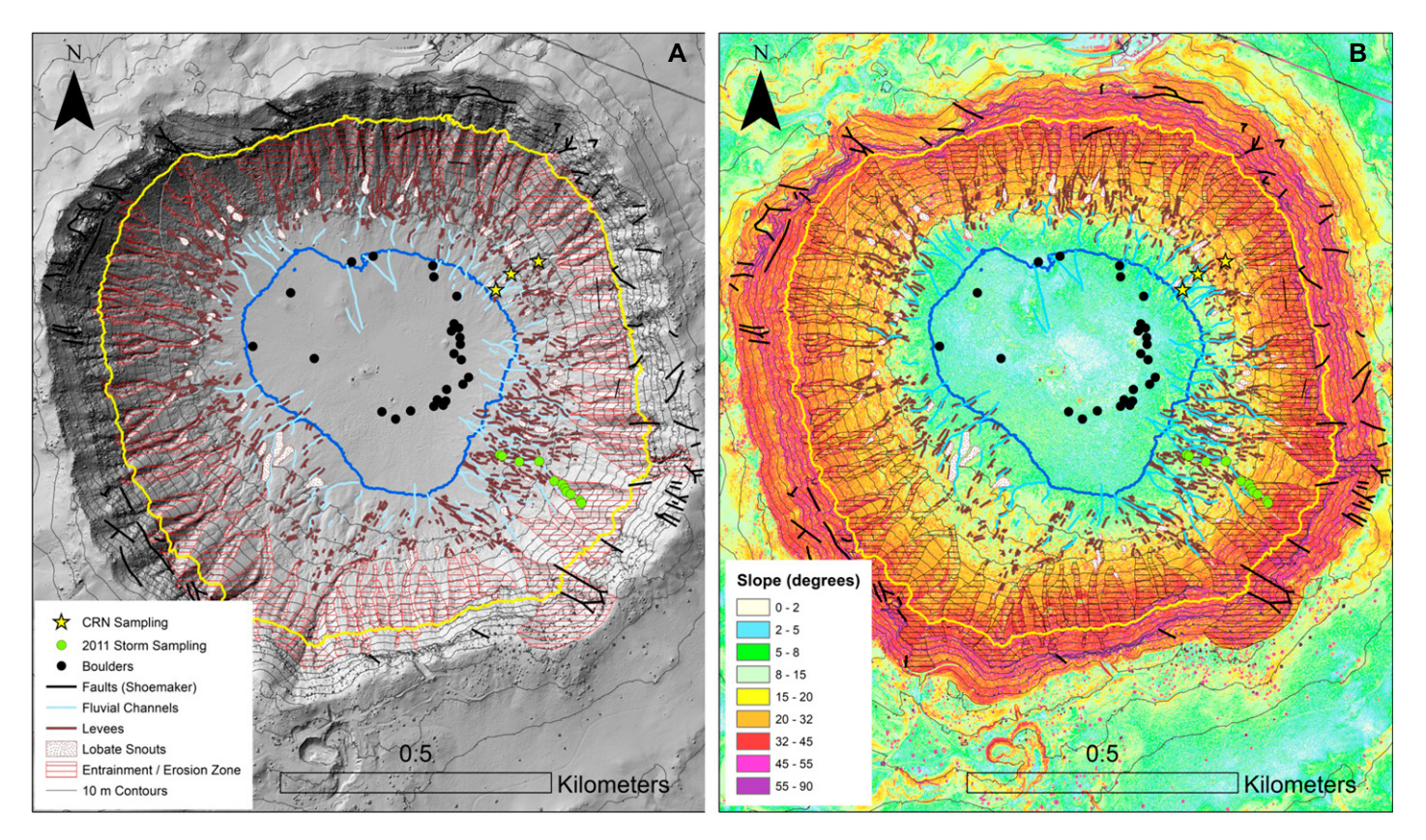


Figure 3. (A) Geomorphic map of Meteor Crater overlain on shaded relief image. Blue contour shows the highest mapped extent of the Pleistocene lake, and yellow contour shows the average elevation where gully incision begins. (B) Same geomorphic map as in panel A, except with a slopeshade image underlain to highlight the slope dependence of different erosional and depositional landforms. CRN—cosmogenic radionuclide.

bar forms within a channel. The spatial distributions of channels, boulder snouts, and levees and the crosscutting relationships among deposits were identified and mapped onto 25 cm contour data in the field, which informed subsequent mapping. Using a handheld global positioning system (GPS) and LiDAR data, we also identified the lowest position of boulders on the crater floor. Fluvial channel cross sections and debris-flow tracks were surveyed in the field; these surveys were used to estimate levee volumes for comparison with the volume estimates performed using the LiDAR data alone.

Following a monsoonal storm in early September 2011, we noted the occurrence of fluvial channel development on the floor of many gullies (i.e., where runoff incised V-shaped, slightly meandering channels, often with small gravel bars, on the floor of previous debris-flow tracks). Within "gully 16" (Fig. 3A), where a mostly continuous fluvial channel developed from the headwall to the crater floor, we collected data on bankfull channel dimensions, channel slope, and grain size at each of the points (green dots) marked in Figure 3A. We measured fluvial channel width (w) and bankfull depth (h) in the field, and the local slope was calculated over 10 m (5 m upstream and downstream of the channel cross section). The upslope drainage area from each of these sites was calculated using LiDAR data. For grain size, we conducted Wolman pebble counts (e.g., Wolman, 1954; Bunte and Abt, 2001) on bars that developed in the fluvial channels to determine the critical discharge for fluvial sediment motion and the source area runoff rate. To conduct these counts, we set up grids and measured the intermediate axis of the particle at each grid node, with the particle being chosen using the tip of a mechanical pencil, making sure to count at least 100 grains for the determination of the median grain size  $(D_{50})$  and  $D_{84}$  (i.e., the grain size at which 84% of the grains are smaller) within tolerable limits (Wolman, 1954).

### Fluvial Runoff and Sediment Transport Formulation

Instantaneous storm discharge (*Q*) and corresponding runoff rates (i.e., discharge divided by the upslope drainage area) for the September 2011 storm event were estimated at each channel cross section (green dots in Fig. 3A) using principles of continuity:

$$Q = a_{xs}U, (1)$$

where  $a_{xs}$  is the flow cross-sectional area (estimated as the channel width, w, multiplied by the bankfull flow depth, h), and U is the average flow

velocity. The average flow velocity was calculated using the Darcy-Weisbach equation:

$$U = \sqrt{\frac{8ghS}{f}},\tag{2}$$

where g is gravity (9.8 m/s $^2$ ), S is the fluid surface slope, and f is the Darcy-Weisbach friction factor, a quantification of flow resistance. For channels with width-to-depth ratios less than 20, the hydraulic radius,  $R_h$ , which is the ratio of the channel area (wh) to its wetted perimeter (2 h + w), was used instead of h in Equation 2. We assumed uniform flow such that the fluid surface slope equaled the local tangent of the bed slope angle,  $\theta$ . Local bed slope was extracted from our LiDAR-derived digital elevation models (DEMs) from long profiles that extended 5 m upstream and 5 m downstream of each cross section. Ferguson (2007) derived an empirical expression for f that was intended to work for a range of flow conditions and channel slopes:

$$\sqrt{\frac{8}{f}} = 17.7 \frac{h}{D_{84}} \frac{1}{\sqrt{52.3 + 5.57 \left(\frac{h}{D_{84}}\right)^{5/3}}}.$$
 (3)

In order to estimate modern-day sediment fluxes transported by fluvial processes from the crater wall to its floor, we used an empirical model by Schneider et al. (2015). This model was developed using field data from sites that covered a wide range of channel bed slopes, grain sizes, and water discharges, and it accounts for bed forms and other sources of macroscale roughness that can affect flow resistance and resulting sediment fluxes. This model was found to best predict sediment motion in a fine gravel-bed channel on an alluvial fan with slopes similar to those at Meteor Crater (Palucis et al., 2023). In this model, the nondimensional transport rate  $(W^*)$  is a function of both (1) the median grain size  $(D_{50})$  of the coarse grain-size distribution (grains >4 mm) and (2) the ratio of the total dimensionless boundary shear stress on the bed  $(\tau^*)$  to the reference shear stress  $(\tau_r^*)$ , where the reference shear stress  $\tau_r^*$  is defined as

$$\tau_r * = 0.56S^{0.5}, \tag{4}$$

and the boundary shear stress on the bed is

$$\tau^* = \frac{\tau_b}{(\rho_s - \rho)gD_{50}} = \frac{\rho g R_h S}{(\rho_s - \rho)gD_{50}}.$$
 (5)

The nondimensional bed-load transport model is

$$W_{tot}^* = \begin{cases} 0.002(\tau^*/\tau_r^*)^{16.1} & \text{for } \tau^*/\tau_r^* \\ < 1.2 & \text{and } D_{50} > 4 \text{ mm} \\ 14\left(1 - \frac{0.85}{(\tau^*/\tau_r^*)^{0.7}}\right)^{4.5} & \text{for } \tau^*/\tau_r^* \end{cases}$$
(6) 
$$\geq 1.2 \text{ and } D_{50} > 4 \text{ mm}$$

We then converted dimensionless transport rates to volumetric bed-load transport rates ( $q_{\text{Vol}}$ ) per unit width (m³ s<sup>-1</sup> m<sup>-1</sup>) using

$$q_{Vol} = \frac{W_{tot}^* u_*^3}{\Re \sigma},\tag{7}$$

where  $u^* = \sqrt{\tau_b/\rho}$  is the shear velocity, and  $\Re$  is the submerged density of quartz (1.65).

### <sup>10</sup>Be/<sup>26</sup>Al Exposure Dating

To determine the timing of debris-flow activity at Meteor Crater (via levee emplacement), we collected four samples from levee deposits associated with gully 0, labeled MC-11-01 through MC-11-04 (Fig. 4). The samples were derived from sandy dolomite blocks (Kaibab Formation), which consisted chiefly of dolomite with various amounts of detrital and secondary quartz. They were chosen because they were expected to be the most resistant to weathering and have the most continuous exposure ages. Maximum sample depth from the exposed surfaces was 1.5 cm. All samples, except one (MC-11-04), were collected from relatively flat horizontal surfaces; MC-11-04 was collected on a vertical face to test for shielding effects on the same boulder as MC-11-03. The sampled deposits were located downslope from a weathering-resistant, thumbshaped knob rising above the oldest Pleistocene talus near the base of the beta member of the Kaibab Formation; this knob was also sampled by Nishiizumi et al. (1991) (M-01, Fig. 4).

Prior to the impact, the  $\sim$ 250-m.y.-old Kaibab dolomite was shielded by  $\sim$ 8–10 m of Moenkopi sandstone, such that production rates of <sup>10</sup>Be would be on the order of  $1 \times 10^{-6}$  atoms/g/yr (surface rates based on geographic latitude). At this production rate, any inherited <sup>10</sup>Be would be  $\sim$ 0.1% of the total  $^{10}$ Be measured in each sample (Table 1). Once the impact occurred, the rocks we sampled were likely exposed to cosmogenic radiation, but presumably under different shielding conditions. When choosing our samples, we looked for rocks that appeared to be in place (i.e., had not recently been overturned or moved) and minimally eroded, allowing for a greater chance that they were not exposed at the surface for a long time before being entrained and deposited by a debris flow.

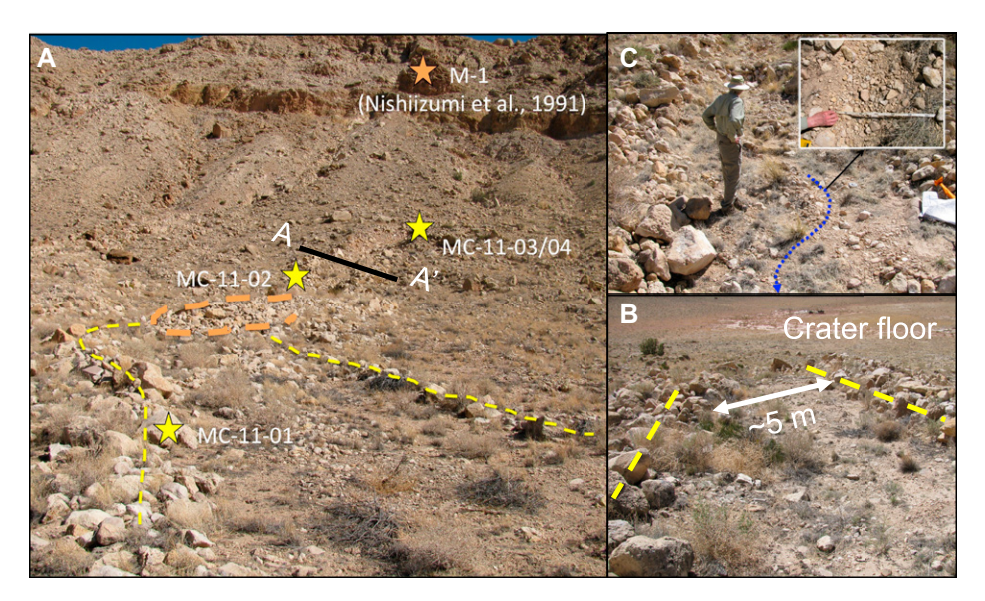


Figure 4. (A) Sampling locations (yellow stars) within gully 0 for <sup>10</sup>Be cosmogenic dating of coarse-grained levee deposits (yellow dashed lines). A lobate deposit is traced in orange. Cross section A–A′ is shown in Figure 5B. (B) An ~5-m-wide, debris flow–created channel between debris-flow levees. (C) Location where grain-size data were collected in gully 0; the low-flow fluvial channel is highlighted with a dashed blue line, and the low-flow fluvial channel bed is shown in the inset panel.

TABLE 1. RESULTS FROM  $^{10}$ Be AND  $^{26}$ AI COSMOGENIC NUCLIDE DATING OF THE LEVEE DEPOSITS AT GULLY 1, METEOR CRATER, ARIZONA

Sample name	Elevation (m)	Mass (g)	<sup>10</sup> Be/Be (E-15)	<sup>26</sup> Al/Al (E-15)	Be-10 (atoms/g)	Al-26 (atoms/g)	Exposure age (1000 yr)
M-1	1680	30.261	114.8	490	0.425 E + 06	.275 E + 07	28.85 + 1.47
MC-11-01	1564	49.925	720.8	0	0.189 E + 06	0	13.91 + 0.67
MC-11-02	1580	50.306	983.5	0	0.257 E + 06	0	18.66 + 1.23
MC-11-03	1600	50.368	539.1	0	0.140 E + 06	0	10.05 + 0.38
MC-11-04	1600	50.232	397	0	0.104 E + 06	0	7.42 + 0.31

The samples were processed to obtain a pure quartz phase, and then the Be and Al were chemically separated and purified (Kohl and Nishiizumi, 1992). The <sup>10</sup>Be and <sup>26</sup>Al measurements were obtained using accelerator mass spectrometry (AMS) at the Purdue Rare Isotope Measure-

ment (PRIME) Laboratory. Exposure ages were calculated for these samples using production rates of <sup>10</sup>Be and <sup>26</sup>Al at sea level (>50° latitude) of 6.0 and 36.8 atoms/g/yr of SiO<sub>2</sub>, respectively (Nishiizumi et al., 1989), and correcting for sample altitude, latitude, and exposure geometry (Lal and Peters, 1967). We used the geographic latitude to calculate exposure ages since the present geomagnetic latitude is not the same as it was during the last 50,000 yr. We estimated an overall uncertainty of about  $\pm 10\%$  in the production rates of these nuclides (Nishiizumi et al., 1989). Exposure ages were calculated assuming no erosion, but we acknowledge that most surfaces experience some erosion with continuous exposure (though no soil development was observed on the rocks we sampled). By making a "no erosion" assumption, our ages are defined to be minimum exposure ages. These ages also assume no snow cover on the rocks sampled. Correction for snow cover is negligible at the present time but could possibly have been important in the past.

### **OBSERVATIONS**

#### Gully 0: Model Gully System

Gully 0, located near the northeastern corner of the crater (Figs. 4 and 5; Fig. S3), was chosen to map in detail because of its well-preserved deposits (which we also sampled for cosmogenic radionuclide [CRN] dating) and its location under a prominent bedrock outcrop that was dated by Nishiizumi et al. (1991). The relief at this site is  $\sim 169$  m (from the crater floor to its rim), of which the top  $\sim 76$  m section is exposed bedrock with an average slope of  $35^{\circ}$ . Below

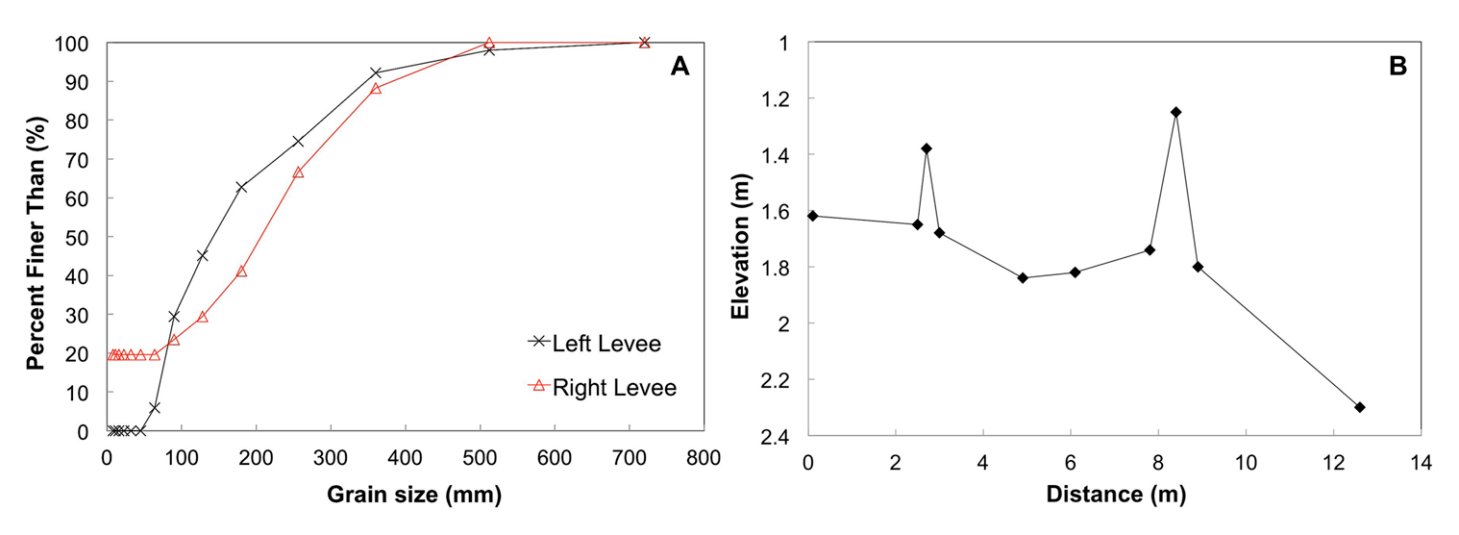


Figure 5. (A) Grain-size distribution of the levee deposits, located near MC-11-02 in gully 0. Right levee (looking downslope) distribution is shown in red, and left levee is shown in black. (B) Cross section, performed in the field, of a levee deposit in gully 0. Location of the cross section is shown in Figure 4A (A-A', black line).

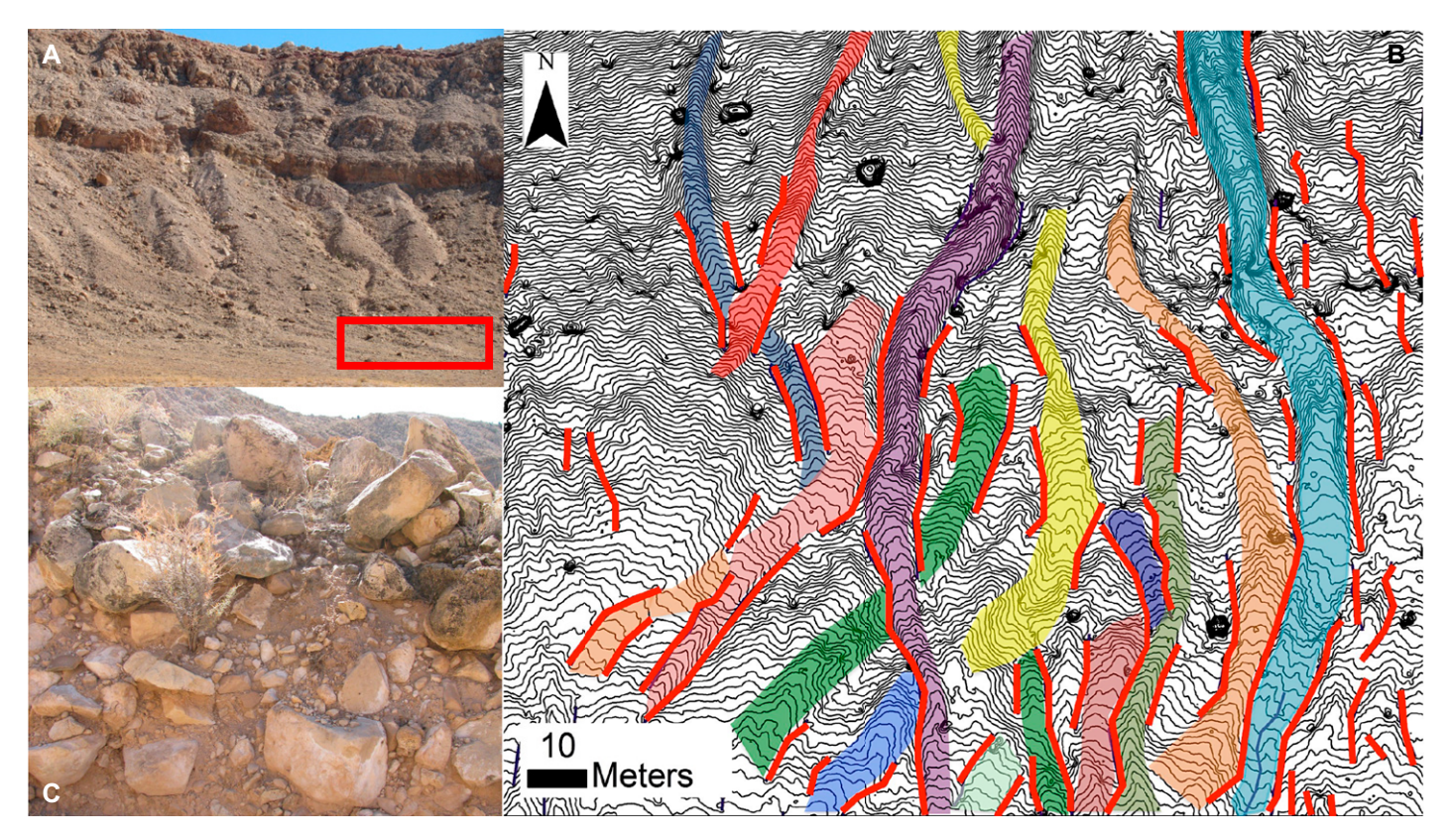


Figure 6. (A) Gully systems on north-northeastern side of the crater; red box shows mapping location in B. The crater wall is ~175 m tall. (B) Topographic map (0.5 m contours) of levee-lined channels (channels are shown in solid colors, and levee deposits are shown in red lines), where each channel is color-coded differently to show the sinuous, crossing, "noodle-like" nature of the debris-flow channels within Meteor Crater. The flow direction is approximately south. (C) Lateral deposit found in gully 0 showing poorly sorted, matrix-supported clasts indicative of mass-flow processes. The largest clasts are ~30 to 50 cm in length.

the bedrock, there is an  $\sim$ 53 m section of talus, composed mostly of impact breccia and rockfall from the bedrock cliffs above. There is an amphitheater-shaped alcove (gully head) where the talus is incised that has steep ( $\sim 33^{\circ}-35^{\circ}$ ) sidewall slopes. The average depth of the alcove is  $\sim$ 3.7 m. Downslope of the talus, there is an undulating surface (~10 m in relief) with an average slope of  $\sim$ 7°, marked by crisscrossing boulder-laced, lobate snouts and debris-flow tracks (Fig. 5B). Some of the boulders within the levees of the debris-flow tracks showed evidence of having a calcium carbonate coating on them before being entrained in the flow, which allowed us to trace the source of these coated boulders to a local knickpoint in the gully. Exposures in the walls of the levees (Fig. 5C) show them to be predominantly matrix-supported, though careful digging into the deposits revealed isolated regions of stratified sand and gravel, suggesting minor fluvial deposition. The matrix was predominantly sandy, though finer-grained black material, possibly ash from eruptions in the nearby San Francisco volcanic field (Conway et al., 1998), was observed.

We surveyed an especially well-preserved pair of levees leading to a lobate deposit that likely defined a single debris-flow event; this event crossed a preexisting, visually older pair of levees created by another debris flow that had run farther out (see Fig. 4). In both flows, the levee deposits are  $\sim$ 5 m apart and  $\sim$ 0.4–0.7 m high (Fig. 6) and are detectable in the LiDAR data. The local depositional slope for both flows was  $\sim 5^{\circ}$ . In addition to surficial evidence for debris flows, we observed an ~4-m-wide and 15-cm-deep channel with a gravel bar ( $D_{50}$  $\sim$ 50 mm) between the level deposits on the gully floor. The V-shaped contours of this channel were detectable in the 25 cm LiDAR data. Incised into this "high-flow" channel, there was a smaller "low-flow," 0.4-m-wide channel (Fig. 4C); a pebble count on a bar in the smaller channel gave a median grain size of 22 mm. The smaller channel appeared to be from a recent event (prior to May 2011) based on disturbances to the vegetation (i.e., flattening of the vegetation in the downslope direction).

Kumar and Kring (2008) had proposed that groundwater seepage was the main source of

water driving gully incision in Meteor Crater. Our field observations at this gully system (and elsewhere across the crater) do not support this hypothesis. At the headwall of the gully, there was no evidence of staining or coarse gravel lag deposits, and no evidence for sustained fluvial wash in the channel. We also did not see any caves or large fractures from which groundwater would have discharged, though smaller fractures and joints with  $\sim 1-3$  m spacing occur regularly in the Kaibab Formation due to uplift of the Colorado Plateau (Roddy, 1978; Shoemaker, 1987; Kring, 2007). We did observe channel development within the bedrock cliffs above the talus (white arrows, Fig. 2B), suggesting that during storm events, water from precipitation (rain or snowmelt) concentrates and flows over the steep bedrock cliffs onto the talus below, where it entrains sediment. In the neighboring nongullied talus, we did not observe evidence of landsliding processes (e.g., landslide scars, headscarps, rotational blocks, etc.), nor did we observe more than minor rilling within the talus, both suggestive that gully incision was predominately from runoff off bedrock and sediment entrainment.

## Morphometric Analysis of Gully Systems at Meteor Crater

Using our observations from gully 0, as well as several neighboring gullies, we were able to correlate features on the ground (i.e., levees, small fluvial channels, and lobate debris-flow

deposits) with their topography on the LiDAR map. We characterized the morphology of 71 individual gully systems within Meteor Crater (Fig. S4) using a combination of field mapping and LiDAR analysis, as reported in Table 2. Almost all the gullies at Meteor Crater begin at approximately the same elevation around

TABLE 2. MORPHOMETRIC PARAMETERS OF GULLIES WITHIN METEOR CRATER, ARIZONA

(m²) (m̂) (m̂) (m̂) (m̄) (m̄) (m̄) (m̄) (m̄) (m̄) (m̄) (m̄	ORIG FID	Head area	Depth	Volume	Length	Gully floor slope	Elevation of
(m)  1	OTTIG_T ID						
07		( )	()	( )	()	( )	
1	0*	2759*	3 71*	10 230*	153*	279*	. ,
2	1				116		
10	2	4517		16,894	104	26.1	1659
10	3				108	24.1	1650
10	4						1690
10	5						1635
10	7						1632
10	8						
11		1274	2.99	3804	106	19.8	1633
122 1945 0.96 1874 101 30.3 1661 133 916 2.40 1400 116 25.5 1650 144 4514 1.78 8021 192 22.9 1671 15 6329 4.67 27.562 123 21.6 1660 16† 9736† 3.70† 35.985† 193† 23.8† 1683† 17 3260 5.02 16,347 108 22.6 1641 18 4924 5.25 35.848 159 24.8 1670 19 14,087 6.74 94,900 237 19.4 1697 200 2741 2.88 7883 136 24.7 1659 221 1065 122 1294 110 23.2 1658 22 3028 1.94 5874 112 24.8 1647 23.2 1294 110 23.2 1658 22 3028 1.94 5874 112 24.8 1647 24.2 24.2 24.2 24.2 2842 3.82 10,845 116 28.2 1665 25 1941 2.51 4871 99 24.2 1658 26 2023 4.78 9678 97 24.4 1659 267 1521 0.85 1290 163 27.8 1661 282 210 1.01 13.003 112 26.9 1658 29 4781 2.72 13,003 158 23.4 1661 303 14,404 6.23 92.637 220 23.6 1662 29 4781 2.75 33 4564 7613 151 29.1 1667 33 4981 7654 7670 24.5 1667 24.6 1672 33 4981 7654 7613 151 29.1 1667 33 4981 7654 7613 151 29.1 1667 33 4981 7654 7613 151 29.1 1667 33 4981 7654 7613 37 47 57 58 73.9 37,563 171 25 1663 32.4 1661 33 4981 7654 7611 31 151 24.6 1672 34 1576 2.61 4116 68 20.1 1619 33 4981 7654 76113 151 24.6 1672 34 1576 2.61 4116 68 20.1 1619 35 4881 4980 3.57 17,762 132 22.9 1658 24.8 1662 36 3608 6.84 24.697 123 21.8 1657 33 4981 7654 76113 151 24.6 1672 36 36 3608 6.84 24.697 123 21.8 1657 33 4981 7654 77,70 156 24.8 1672 33 476 476 113 151 24.6 1672 36 36 3608 6.84 24.697 123 22.9 1658 24.8 1662 36 3608 6.84 24.697 123 21.8 1657 33 33 4981 7654 7613 151 24.6 1672 36 36 3608 6.84 24.697 123 21.8 1657 36 36 3608 6.84 24.697 123 22.9 1658 44 1576 2.61 4116 68 20.1 1619 35 6887 2.47 17,005 150 24.5 1662 36 3608 6.84 24.697 123 21.8 1657 36 36 36 3608 6.84 24.697 123 22.9 1658 25.7 1669 25.5 1668 25.7 1669 25.5 1669 25.5 1668 25.7 1669 25.5 1668 25.7 1669 25.5 1669 25.5 1669 25.7 1669 25.5 1669 25.7 1669 25.	10				82		1641
13							16//
144         4514         1.78         8021         192         22.9         1671           15         6329         4.67         27,562         123         21.6         1660           16†         9736†         3.70¹         35,985†         193¹         23,8¹         1883¹           17         3260         5.02         16,347         108         22.6         1641           18         4924         5.25         35,848         159         24.8         1670           19         14,087         6,74         94,900         237         19.4         1897           20         2741         2.88         7883         136         24.7         1659           21         1065         122         1294         110         23.2         1658           22         3028         19.4         20.611         113         29.4         1670           24         2842         3.82         10,845         116         28.2         21665           25         1941         2.51         4871         99         24.2         1686           25         1941         2.51         4877         94.9         97         24							
15         6329         4.67         27,562         123         21.6         1660           16†         9736†         3.70*         35,985†         193*         23.8¹         1683†           17         3260         5.02         16,347         108         22.6         1641           18         4924         5.25         35,848         159         24.8         1670           19         14,087         6.74         94,900         237         19.4         1697           20         2741         2.88         7883         136         24.7         1669           21         1065         1.22         1294         110         23.2         1658           22         3028         1.94         5874         112         24.8         1647           23         4175         4.94         20.611         113         29.4         1670           24         2842         3.82         10.845         116         28.2         21665           25         1941         2.51         4871         199         24.2         1658           26         2023         4.78         9678         97         24.4         1	14						1671
17         3260         5.02         16,347         108         22.6         1641           18         4924         5.25         35,848         159         24.8         1670           19         14,087         6.74         94,900         237         19.4         1697           20         2741         2.88         7883         136         24.7         1659           21         1065         1.22         1294         110         23.2         1658           22         3028         1.94         5874         112         24.8         1677           23         4175         4.94         20,611         113         29.4         1670           24         2842         3.82         10,845         116         28.2         1658           255         1941         2.51         4871         99         24.2         1658           265         2023         4.78         9678         97         24.4         1659           27         1521         0.85         1290         163         27.8         1661           282         2210         1.01         13.003         152         26.9         1658	15	6329	4.67	27,562	123	21.6	1660
18         4924         5.25         35,848         159         24.8         1670           19         14,087         6,74         94,900         237         19.4         1697           20         2741         2.88         7883         136         24.7         1659           21         1065         1.22         1294         110         23.2         1658           22         3028         1.94         5874         112         24.8         1647           23         4175         4.94         20.611         113         29.4         1670           24         2842         3.82         10,845         116         28.2         1665           255         1941         2.51         4871         99         24.2         1658           25         1941         2.51         4871         99         24.2         1658           25         1941         2.51         4871         99         24.2         1658           25         1941         2.51         4871         99         24.2         1658           25         1941         2.51         481         1867         24.4         1659 <td>16<sup>†</sup></td> <td></td> <td></td> <td></td> <td></td> <td>23.8<sup>†</sup></td> <td>1683<sup>†</sup></td>	16 <sup>†</sup>					23.8 <sup>†</sup>	1683 <sup>†</sup>
19							1641
20					237		1670
222 3028 1.94 5874 112 24.8 1647 233 4175 4.94 20.611 113 29.4 1670 244 2842 3.82 10.845 116 28.2 1665 255 1941 2.51 4871 99 24.2 1658 266 2023 4.78 9678 97 24.4 1659 27 1521 0.85 1290 163 27.8 1661 28 2210 1.01 13.003 158 23.4 1661 28 2210 1.01 13.003 158 23.4 1661 28 29 4781 2.72 13.003 158 23.4 1661 28 301 14.404 6.23 92.637 220 23.6 1662 301 7578 739 37.563 171 25 1663 303 4981 764 76.113 151 24.6 1672 303 4981 764 76.113 151 24.6 1672 304 1576 2.61 4116 68 20.1 1619 305 6887 2.47 17.005 150 24.5 1662 307 333 4981 764 76.113 151 24.6 1672 308 3608 6.84 24.697 123 21.8 1657 309 37.563 177 3008 6.8 20.1 1619 309 726 0.67 489 99 26.8 1660 309 726 0.67 489 199 26.8 1660 310 13.40 2.50 13.3 751 54 31.6 1661 311 3780 4.49 14.864 133 25.7 1668 311 3780 4.49 14.864 133 25.7 1668 311 3780 4.49 14.864 133 25.7 1668 311 3780 4.49 14.864 133 25.7 1668 311 3780 4.49 14.864 133 25.7 1668 311 3780 4.49 14.864 133 25.7 1668 311 3780 4.49 14.864 133 25.7 1668 311 3780 4.49 14.864 133 25.7 1668 311 3780 4.49 14.864 133 25.7 1668 311 3116 1524 3.24 4932 92 29.8 1659 311 3146 1.16 1326 93 33.1 1661 318 499 90 3.57 1762 122 26.2 1654 319 90 3 1.34 1210 87 273 1658 319 90 30 1.34 1210 87 273 1658 319 90 30 1.34 1210 87 273 1658 319 90 30 1.34 1210 87 273 1653 319 90 30 1.34 1210 87 273 1653 319 90 30 1.34 1210 87 273 1653 319 90 30 1.34 1210 87 273 1653 319 90 30 1.34 1210 87 273 1653 319 90 30 1.34 1210 87 273 1653 310 1340 1.72 2308 83 29.9 1651 3147 4.20 11.011 101 31.5 1657 314 1331 1.89 2510 93 28.3 1660 3140 1.72 2308 83 29.9 1651 3150 1.72 2308 83 29.9 1651 31660 1340 1.72 2308 83 29.9 1651 3160 1340 1.72 2308 83 29.9 1651 317 1.75 1.76 1.76 1.77 1.76 1.77 1.77 1.77 1.77					136		
222 3028 1.94 5874 112 24.8 1647 233 4175 4.94 20.611 113 29.4 1670 244 2842 3.82 10.845 116 28.2 1665 255 1941 2.51 4871 99 24.2 1658 266 2023 4.78 9678 97 24.4 1659 27 1521 0.85 1290 163 27.8 1661 28 2210 1.01 13.003 158 23.4 1661 28 2210 1.01 13.003 158 23.4 1661 28 29 4781 2.72 13.003 158 23.4 1661 28 301 14.404 6.23 92.637 220 23.6 1662 301 7578 739 37.563 171 25 1663 303 4981 764 76.113 151 24.6 1672 303 4981 764 76.113 151 24.6 1672 304 1576 2.61 4116 68 20.1 1619 305 6887 2.47 17.005 150 24.5 1662 307 333 4981 764 76.113 151 24.6 1672 308 3608 6.84 24.697 123 21.8 1657 309 37.563 177 3008 6.8 20.1 1619 309 726 0.67 489 99 26.8 1660 309 726 0.67 489 199 26.8 1660 310 13.40 2.50 13.3 751 54 31.6 1661 311 3780 4.49 14.864 133 25.7 1668 311 3780 4.49 14.864 133 25.7 1668 311 3780 4.49 14.864 133 25.7 1668 311 3780 4.49 14.864 133 25.7 1668 311 3780 4.49 14.864 133 25.7 1668 311 3780 4.49 14.864 133 25.7 1668 311 3780 4.49 14.864 133 25.7 1668 311 3780 4.49 14.864 133 25.7 1668 311 3780 4.49 14.864 133 25.7 1668 311 3116 1524 3.24 4932 92 29.8 1659 311 3146 1.16 1326 93 33.1 1661 318 499 90 3.57 1762 122 26.2 1654 319 90 3 1.34 1210 87 273 1658 319 90 30 1.34 1210 87 273 1658 319 90 30 1.34 1210 87 273 1658 319 90 30 1.34 1210 87 273 1653 319 90 30 1.34 1210 87 273 1653 319 90 30 1.34 1210 87 273 1653 319 90 30 1.34 1210 87 273 1653 319 90 30 1.34 1210 87 273 1653 319 90 30 1.34 1210 87 273 1653 310 1340 1.72 2308 83 29.9 1651 3147 4.20 11.011 101 31.5 1657 314 1331 1.89 2510 93 28.3 1660 3140 1.72 2308 83 29.9 1651 3150 1.72 2308 83 29.9 1651 31660 1340 1.72 2308 83 29.9 1651 3160 1340 1.72 2308 83 29.9 1651 317 1.75 1.76 1.76 1.77 1.76 1.77 1.77 1.77 1.77	21				110		
24	22				112		
25         1941         2.51         4871         99         24.2         1658           26         2023         4.78         9678         97         24.4         1659           27         1521         0.85         1290         163         27.8         1661           28         2210         1.01         13,003         112         26.9         1658           29         4781         2.72         13,003         158         23.4         1661           30         14,404         6.23         92,637         220         23.6         1662           31         7578         7.39         37563         171         25         1663           32         5072         7.50         38,018         121         29.1         1670           34         1576         2.61         476,113         151         24.6         1672           34         1576         2.61         4116         68         20.1         1619           35         6887         2.47         17,005         150         24.5         1662           36         3608         6.84         24,697         123         21.8         1657	23						
26         2023         4.78         9678         97         24.4         1659           27         1521         0.85         1290         163         228         1661           28         2210         1.01         13.003         112         26.9         1658           29         4781         2.72         13.003         158         23.4         1661           300         14,404         6.23         92,637         220         23.6         1662           31         7578         7.39         37,563         171         25         1663           32         5072         7.50         38.018         121         29.1         1670           33         4981         7.64         76,113         151         24.6         1672           334         1576         2.61         4116         68         20.1         1619           35         6887         2.47         17,005         150         24.5         1662           36         3608         6.84         24,697         123         21.8         1657           37         3337         1.73         5770         156         24.8         1672	24						1659
27         1521         0.85         1290         163         2.78         1661           28         2210         1.01         13,003         112         26.9         1658           229         4781         2.72         13,003         158         23.4         1661           30         14,404         6.23         92,637         220         23.6         1662           31         7578         7.39         37,563         171         25         1663           32         5072         750         38,018         121         29.1         1670           33         4981         764         76,113         151         24.6         1672           34         1576         2.61         4116         68         20.1         1619           35         6887         2.47         17,005         150         24.5         1662           36         3608         6.84         24,697         123         21.8         1657           37         3337         1.73         5770         156         24.8         1672           38         4980         3.57         17,762         132         22.9         1658 <td>26</td> <td></td> <td></td> <td></td> <td>97</td> <td></td> <td>1659</td>	26				97		1659
29         4781         2.72         13,003         158         23.4         1661           30         14,404         6.23         92,637         220         23.6         1662           31         7578         7.50         38,018         121         29.1         1670           32         5072         7.50         38,018         121         29.1         1670           33         4981         7.64         76,113         151         24.6         1672           34         1576         2.61         4116         68         20.1         1619           35         6887         2.47         17,005         150         24.5         1662           36         3608         6.84         24,697         123         21.8         1657           37         3337         1.73         5770         156         24.8         1672           38         4980         3.57         17,762         132         22.9         1658           39         726         0.67         489         99         26.8         1660           40         2130         3.25         6917         103         23.7         1658	27						1661
30       14,404       6,23       92,637       220       23.6       1662         31       7578       7.39       37,563       171       25       1663         32       5072       7.50       38,018       121       29.1       1670         33       4981       7.64       76,113       151       24.6       1672         34       1576       2.61       4116       68       20.1       1619         35       6887       2.47       17,005       150       24.5       1662         36       3608       6.84       24,697       123       21.8       1657         37       3337       1.73       5770       156       24.8       1672         38       4980       3.57       17,762       132       22.9       1658         39       726       0.67       489       99       26.8       1660         40       2130       3.25       6917       103       23.7       1658         41       3780       4.49       14,864       133       25.7       1668         42       1409       2.60       4200       70       29.5       1640     <	28						1658
31         7578         7.39         37,563         171         25         1663           32         5072         7.50         38,018         121         29.1         1670           33         4981         7.64         76,113         151         24.6         1672           34         1576         2.61         4116         68         20.1         1619           35         6887         2.47         17005         150         24.5         1662           36         3608         6.84         24,697         123         21.8         1657           37         3337         1.73         5770         156         24.8         1672           38         4980         3.57         17,762         132         22.9         1658           39         726         0.67         489         99         26.8         1660           40         2130         3.25         6917         103         23.7         1658           41         3780         4.49         14,864         133         25.7         1668           42         1409         2.60         4200         70         29.5         1640 <td></td> <td></td> <td></td> <td></td> <td></td> <td></td> <td>1661</td>							1661
32							
33						29 1	1670
35 6887 2.47 17,005 150 24.5 1662 366 3608 6.84 24,697 123 21.8 1657 37 3337 1.73 5770 156 24.8 1672 38 4980 3.57 17,762 132 22.9 1658 39 726 0.67 489 99 26.8 1660 40 2130 3.25 6917 103 23.7 1668 41 3780 4.49 14,864 133 25.7 1668 42 1409 2.60 4200 70 29.5 1640 43 1146 1.16 1326 93 33.1 1661 44 563 1.33 751 54 31.6 1656 45 1614 1.31 2112 92 26.2 1654 46 1524 3.24 4932 92 29.8 1659 47 1842 2.94 5413 101 31.1 1658 49 903 1.34 1210 87 273 1658 49 903 1.34 1210 87 273 1658 50 4405 2.73 11,111 153 26 1653 51 2942 2.81 8262 162 18.5 1654 52 2319 6.19 14,344 90 25.5 1661 53 2857 4.98 14,229 102 25.9 1648 553 2857 4.98 14,229 102 25.9 1648 564 1331 1.89 2510 93 28.3 1660 555 1899 0.74 1407 122 24.7 1676 566 3147 4.20 11,011 101 31.5 1657 577 1376 2.22 3055 78 27.5 1648 58 1213 3.02 3661 74 22 14.7 1660 560 1340 1.72 2308 83 29.9 1651 561 9.75 1376 2.22 3055 78 27.5 1648 562 1203 2.17 2615 56 32.7 1660 564 1381 0.98 1357 98 27.8 1660 565 566 1.55 874 49 30.5 1630 666 200 2.52 800 62 28 1668 668 693 3.31 2293 59 35.7 1668 669 640 0.95 609 78 24.9 1645 670 975 2.24 2184 69 33.7 1669	33			76,113		24.6	1672
36         3608         6.84         24,697         123         21.8         1657           37         3337         1.73         5770         156         24.8         1672           38         4980         3.57         17,762         132         22.9         1658           39         726         0.67         489         99         26.8         1660           40         2130         3.25         6917         103         23.7         1658           41         3780         4.49         14,864         133         25.7         1668           42         1409         2.60         4200         70         29.5         1640           43         1146         1.16         1326         93         33.1         1661           444         563         1.33         751         54         31.6         1656           455         1614         1.31         2112         92         26.2         1654           46         1524         3.24         4932         92         29.8         1659           47         1842         2.94         5413         101         31.1         1658 <t< td=""><td>34</td><td></td><td></td><td></td><td></td><td>20.1</td><td>1619</td></t<>	34					20.1	1619
38         4980         3.57         17,762         132         22.9         1658           39         726         0.67         489         99         26.8         1660           40         2130         3.25         6917         103         23.7         1658           41         3780         4.49         14,864         133         25.7         1668           42         1409         2.60         4200         70         29.5         1640           43         1146         1.16         1326         93         33.1         1661           44         563         1.33         751         54         31.6         1656           45         1614         1.31         2112         92         26.2         1654           46         1524         3.24         4932         92         29.8         1659           47         1842         2.94         5413         101         31.1         1658           49         903         1.34         1210         87         27.3         1653           50         4405         2.73         11,111         153         26         1653					150		
38         4980         3.57         17,762         132         22.9         1658           39         726         0.67         489         99         26.8         1660           40         2130         3.25         6917         103         23.7         1658           41         3780         4.49         14,864         133         25.7         1668           42         1409         2.60         4200         70         29.5         1640           43         1146         1.16         1326         93         33.1         1661           44         563         1.33         751         54         31.6         1656           45         1614         1.31         2112         92         26.2         1654           46         1524         3.24         4932         92         29.8         1659           47         1842         2.94         5413         101         31.1         1658           49         903         1.34         1210         87         27.3         1653           50         4405         2.73         11,111         153         26         1653	36 37				123 156		1657 1672
39         726         0.67         489         99         26.8         1660           40         2130         3.25         6917         103         23.7         1658           41         3780         4.49         14,864         133         25.7         1668           42         1409         2.60         4200         70         29.5         1640           43         1146         1.16         1326         93         33.1         1661           44         563         1.33         751         54         31.6         1656           45         1614         1.31         2112         92         26.2         1654           45         1614         1.31         2112         92         29.8         1659           47         1842         2.94         5413         101         31.1         1658           47         1842         2.94         5413         101         31.1         1658           47         1842         2.94         5413         101         31.1         1658           49         903         1.34         1210         87         27.3         1653					132		
41       3780       4.49       14,864       133       25,7       1668         42       1409       2.60       4200       70       29.5       1640         43       1146       1.16       1326       93       33.1       1661         44       563       1.33       751       54       31.6       1656         45       1614       1.31       2112       92       26.2       1654         46       1524       324       4932       92       29.8       1659         47       1842       2.94       5413       101       31.1       1658         49       903       1.34       1210       87       27.3       1653         50       4405       2.73       11,111       153       26       1653         51       2942       2.81       8262       162       18.5       1654         52       2319       6.19       14,344       90       25.5       1661         53       2857       4.98       14,229       102       25.9       1648         54       1331       1.89       2510       93       28.3       1660	39				99		
42       1409       2.60       4200       70       29.5       1640         43       1146       1.16       1326       93       33.1       1661         444       563       1.33       751       54       31.6       1656         45       1614       1.31       2112       92       26.2       1654         46       1524       3.24       4932       92       29.8       1659         47       1842       2.94       5413       101       31.1       1658         49       903       1.34       1210       87       27.3       1653         50       4405       2.73       11,111       153       26       1653         51       2942       2.81       8262       162       18.5       1654         52       2319       6.19       14,344       90       25.5       1661         53       2857       4.98       14,229       102       25.9       1648         54       1331       1.89       2510       93       28.3       1660         55       1899       0.74       1407       122       24.7       1676	40			6917			1658
43       1146       1.16       1326       93       33.1       1661         444       563       1.33       751       54       31.6       1656         45       1614       1.31       2112       92       26.2       1654         46       1524       3.24       4932       92       29.8       1659         47       1842       2.94       5413       101       31.1       1658         49       903       1.34       1210       87       27.3       1653         50       4405       2.73       11,111       153       26       1653         51       2942       2.81       8262       162       18.5       1654         52       2319       6.19       14,344       90       25.5       1661         52       2319       6.19       14,344       90       25.5       1661         53       2857       4.98       14,229       102       25.9       1648         54       1331       1.89       2510       93       28.3       1660         55       1899       0.74       1407       122       24.7       1676				14,864			1668
44         563         1.33         751         54         31.6         1656           45         1614         1.31         2112         92         26.2         1654           46         1524         3.24         4932         92         29.8         1659           47         1842         2.94         5413         101         31.1         1658           49         903         1.34         1210         87         27.3         1653           50         4405         2.73         11,111         153         26         1653           51         2942         2.81         8262         162         18.5         1654           52         2319         6.19         14,344         90         25.5         1661           53         2857         4.98         14,229         102         25.9         1648           54         1331         1.89         2510         93         28.3         1660           55         1899         0.74         1407         122         24,7         1676           56         3147         4.20         11,011         101         31.5         1657 <tr< td=""><td></td><td></td><td></td><td></td><td></td><td></td><td></td></tr<>							
45         1614         1.31         2112         92         26.2         1654           46         1524         3.24         4932         92         29.8         1659           47         1842         2.94         5413         101         31.1         1658           49         903         1.34         1210         87         27.3         1653           50         4405         2.73         11,111         153         26         1653           51         2942         2.81         8262         162         18.5         1654           52         2319         6.19         14,344         90         25.5         1661           53         2857         4.98         14,229         102         25.9         1648           54         1331         1.89         2510         93         28.3         1660           55         1899         0.74         1407         122         24.7         1676           56         3147         4.20         11,011         101         31.5         1657           57         1376         2.22         3055         78         275         1648 <t< td=""><td>44</td><td></td><td></td><td></td><td></td><td></td><td></td></t<>	44						
47         1842         2.94         5413         101         31.1         1658           49         903         1.34         1210         87         27.3         1653           50         4405         2.73         11,111         153         26         1653           51         2942         2.81         8262         162         18.5         1654           52         2319         6.19         14,344         90         25.5         1661           53         2857         4.98         14,229         102         25.9         1648           54         1331         1.89         2510         93         28.3         1660           55         1899         0.74         1407         122         24.7         1676           56         3147         4.20         11,011         101         31.5         1657           57         1376         2.22         3055         78         27.5         1648           58         1213         3.02         3661         74         22         1628           59         2502         3.42         8552         130         22.4         1660 <t< td=""><td>45</td><td>1614</td><td>1.31</td><td>2112</td><td>92</td><td>26.2</td><td>1654</td></t<>	45	1614	1.31	2112	92	26.2	1654
49         903         1.34         1210         87         27.3         1653           50         4405         2.73         11,111         153         26         1653           51         2942         2.81         8262         162         18.5         1654           52         2319         6.19         14,344         90         25.5         1661           53         2857         4.98         14,229         102         25.9         1648           54         1331         1.89         2510         93         28.3         1660           55         1899         0.74         1407         122         24.7         1676           56         3147         4.20         11,011         101         31.5         1657           57         1376         2.22         3055         78         27.5         1648           58         1213         3.02         3661         74         22         1628           59         2502         3.42         8552         130         22.4         1660           60         1340         1.72         2308         83         29.9         1651 <tr< td=""><td>46</td><td></td><td></td><td>4932</td><td></td><td></td><td></td></tr<>	46			4932			
50         4405         2.73         11,111         153         26         1653           51         2942         2.81         8262         162         18.5         1654           52         2319         6.19         14,344         90         25.5         1661           53         2857         4.98         14,229         102         25.9         1648           54         1331         1.89         2510         93         28.3         1660           55         1899         0.74         1407         122         24.7         1676           56         3147         4.20         11,011         101         31.5         1657           57         1376         2.22         3055         78         27.5         1648           58         1213         3.02         3661         74         22         1628           59         2502         3.42         8552         130         22.4         1660           60         1340         1.72         2308         83         29.9         1651           61         917         1.50         1372         46         27.5         1643 <tr< td=""><td></td><td></td><td></td><td>5413</td><td></td><td>31.1</td><td>1658</td></tr<>				5413		31.1	1658
51         2942         2.81         8262         162         18.5         1654           52         2319         6.19         14,344         90         25.5         1661           53         2857         4.98         14,229         102         25.9         1648           54         1331         1.89         2510         93         28.3         1660           55         1899         0.74         1407         122         24.7         1676           56         3147         4.20         11,011         101         31.5         1657           57         1376         2.22         3055         78         27.5         1648           58         1213         3.02         3661         74         22         1628           59         2502         3.42         8552         130         22.4         1660           60         1340         1.72         2308         83         29.9         1651           61         917         1.50         1372         46         27.5         1643           62         1203         2.17         2615         56         32.7         1660							
52         2319         6.19         14,344         90         25.5         1661           53         2857         4.98         14,229         102         25.9         1648           54         1331         1.89         2510         93         28.3         1660           55         1899         0.74         1407         122         24.7         1676           56         3147         4.20         11,011         101         31.5         1657           57         1376         2.22         3055         78         27.5         1648           58         1213         3.02         3661         74         22         1628           59         2502         3.42         8552         130         22.4         1660           60         1340         1.72         2308         83         29.9         1651           61         917         1.50         1372         46         27.5         1643           62         1203         2.17         2615         56         32.7         1660           63         2786         5.27         10,679         86         29.6         1660 <tr< td=""><td>51</td><td></td><td></td><td></td><td></td><td></td><td>1654</td></tr<>	51						1654
54         1331         1.89         2510         93         28.3         1660           55         1899         0.74         1407         122         24.7         1676           56         3147         4.20         11,011         101         31.5         1657           57         1376         2.22         3055         78         27.5         1648           58         1213         3.02         3661         74         22         1628           59         2502         3.42         8552         130         22.4         1660           60         1340         1.72         2308         83         29.9         1651           61         917         1.50         1372         46         27.5         1643           62         1203         2.17         2615         56         32.7         1660           63         2786         5.27         10,679         86         29.6         1660           64         1381         0.98         1357         98         27.8         1659           65         566         1.55         874         49         30.5         1630	52		6.19	14,344	90	25.5	1661
55         1899         0.74         1407         122         24.7         1676           56         3147         4.20         11,011         101         31.5         1657           57         1376         2.22         3055         78         27.5         1648           58         1213         3.02         3661         74         22         1628           59         2502         3.42         8552         130         22.4         1660           60         1340         1.72         2308         83         29.9         1651           61         917         1.50         1372         46         27.5         1643           62         1203         2.17         2615         56         32.7         1660           63         2786         5.27         10,679         86         29.6         1660           64         1381         0.98         1357         98         27.8         1659           65         566         1.55         874         49         30.5         1630           66         200         2.52         800         62         28         1645           <	53						1648
56         3147         4.20         11,011         101         31.5         1657           57         1376         2.22         3055         78         27.5         1648           58         1213         3.02         3661         74         22         1628           59         2502         3.42         8552         130         22.4         1660           60         1340         1.72         2308         83         29.9         1651           61         917         1.50         1372         46         27.5         1643           62         1203         2.17         2615         56         32.7         1660           63         2786         5.27         10,679         86         29.6         1660           64         1381         0.98         1357         98         27.8         1659           65         566         1.55         874         49         30.5         1630           66         200         2.52         800         62         28         1645           67         322         2.52         810         85         26.8         1668							
58     1213     3.02     3661     74     22     1628       59     2502     3.42     8552     130     22.4     1660       60     1340     1.72     2308     83     29.9     1651       61     917     1.50     1372     46     27.5     1643       62     1203     2.17     2615     56     32.7     1660       63     2786     5.27     10,679     86     29.6     1660       64     1381     0.98     1357     98     27.8     1659       65     566     1.55     874     49     30.5     1630       66     200     2.52     800     62     28     1645       67     322     2.52     810     85     26.8     1668       68     693     3.31     2293     59     35.7     1685       69     640     0.95     609     78     24.9     1645       70     975     2.24     2184     69     33.7     1669							1676
58     1213     3.02     3661     74     22     1628       59     2502     3.42     8552     130     22.4     1660       60     1340     1.72     2308     83     29.9     1651       61     917     1.50     1372     46     27.5     1643       62     1203     2.17     2615     56     32.7     1660       63     2786     5.27     10,679     86     29.6     1660       64     1381     0.98     1357     98     27.8     1659       65     566     1.55     874     49     30.5     1630       66     200     2.52     800     62     28     1645       67     322     2.52     810     85     26.8     1668       68     693     3.31     2293     59     35.7     1685       69     640     0.95     609     78     24.9     1645       70     975     2.24     2184     69     33.7     1669	57						1648
60     1340     1.72     2308     83     29.9     1651       61     917     1.50     1372     46     27.5     1643       62     1203     2.17     2615     56     32.7     1660       63     2786     5.27     10,679     86     29.6     1660       64     1381     0.98     1357     98     27.8     1659       65     566     1.55     874     49     30.5     1630       66     200     2.52     800     62     28     1645       67     322     2.52     810     85     26.8     1668       68     693     3.31     2293     59     35.7     1685       69     640     0.95     609     78     24.9     1645       70     975     2.24     2184     69     33.7     1669	58				74	22	1628
61     917     1.50     1372     46     27.5     1643       62     1203     2.17     2615     56     32.7     1660       63     2786     5.27     10.679     86     29.6     1660       64     1381     0.98     1357     98     27.8     1659       65     566     1.55     874     49     30.5     1630       66     200     2.52     800     62     28     1645       67     322     2.52     810     85     26.8     1668       68     693     3.31     2293     59     35.7     1685       69     640     0.95     609     78     24.9     1645       70     975     2.24     2184     69     33.7     1669	59						
62     1203     2.17     2615     56     32.7     1660       63     2786     5.27     10,679     86     29.6     1660       64     1381     0.98     1357     98     27.8     1659       65     566     1.55     874     49     30.5     1630       66     200     2.52     800     62     28     1645       67     322     2.52     810     85     26.8     1668       68     693     3.31     2293     59     35.7     1685       69     640     0.95     609     78     24.9     1645       70     975     2.24     2184     69     33.7     1669	60						
63     2786     5.27     10,679     86     29.6     1660       64     1381     0.98     1357     98     278     1659       65     566     1.55     874     49     30.5     1630       66     200     2.52     800     62     28     1645       67     322     2.52     810     85     26.8     1668       68     693     3.31     2293     59     35.7     1685       69     640     0.95     609     78     24.9     1645       70     975     2.24     2184     69     33.7     1669							
64     1381     0.98     1357     98     2.78     1659       65     566     1.55     874     49     30.5     1630       66     200     2.52     800     62     28     1645       67     322     2.52     810     85     26.8     1668       68     693     3.31     2293     59     35.7     1685       69     640     0.95     609     78     24.9     1645       70     975     2.24     2184     69     33.7     1669	63						
65     566     1.55     874     49     30.5     1630       66     200     2.52     800     62     28     1645       67     322     2.52     810     85     26.8     1668       68     693     3.31     2293     59     35.7     1685       69     640     0.95     609     78     24.9     1645       70     975     2.24     2184     69     33.7     1669	64	1381	0.98	1357	98	27.8	1659
67 322 2.52 810 85 26.8 1668 68 693 3.31 2293 59 35.7 1685 69 640 0.95 609 78 24.9 1645 70 975 2.24 2184 69 33.7 1669	65						
68     693     3.31     2293     59     35.7     1685       69     640     0.95     609     78     24.9     1645       70     975     2.24     2184     69     33.7     1669	66						
69 640 0.95 609 78 24.9 1645 70 975 2.24 2184 69 33.7 1669							
70 975 2.24 2184 69 33.7 1669	69						
71 581 1.17 679 41 30.2 1633	70	975	2.24	2184	69	33.7	1669
	71						

<sup>\*</sup>Cosmogenic radionuclide (CRN) sampling and mapping.

the crater wall, ~1660 m (see yellow contour in Fig. 3; "Elevation of alcove top" in Table 2), which generally corresponds to the transition from the cliff-forming Kaibab limestone to the underlying talus slopes into which the gullies are incised. The gullies on the southern portion of the crater wall, however, begin at a slightly higher elevation ( $\sim$ 1680 m) where uplift of the Kaibab limestone is higher (Kring, 2007). The water source areas contributing to the gullies ranged from 900 to 14,000 m<sup>2</sup>, with an average of 2460 m<sup>2</sup>. The individual alcoves, which result from the removal of breccia and talus, range from  $\sim$ 0.7 to 7.6 m in depth (average  $\sim$ 3 m) and  $\sim$ 500 to 95,000 m<sup>3</sup> by volume (average  $\sim$ 12,000 m3). The gully channels are "U-shaped" in cross section and typically maintain a constant width, being on average  $\sim$ 7 m wide and  $\sim$ 1 m deep (based on five cross sections per gully channel). They are commonly found to either terminate abruptly without fans or end in a lobate deposit of debris ("lobate snouts" in Fig. 3A). Features suggesting a transition into standing water (i.e., deltaic deposits) were not observed. Incised into the gully channels, there are smaller fluvial channels, as was observed at gully 0. These channels tend to be straight, not sinuous, and are sometimes observed to flow around or through mapped lobate debris deposits.

Like the levee deposits found in gully 0, most levees around Meteor Crater tend to be paired, but unpaired deposits were also mapped. One pair of levees is often found within a larger pair of levees, sometimes there are numerous boulder snouts within a single levee pair, and the levees tend to crosscut one another, all providing evidence that multiple events came down each canyon (e.g., Fig. 5). Cross sections of 100 levees (obtained from LiDAR data) show that they tend to be less than 0.6 m high and  $\sim 2 \text{ m}$ wide. Lobate debris-flow boulder snouts located between paired levees range in depth from 0.4 m to 1.8 m, with a mean of 0.8 m. The volume of material comprising an individual debris-flow event was calculated by identifying levees linked to specific lobate snout deposits. We identified 20 well-defined flow events (i.e., a lobate snout connected to paired levees), and from these, we found flow volumes to range from 10 to 1000 m<sup>3</sup>, with an average of 200 m<sup>3</sup>.

In some cases, levee tracks extend onto the crater floor (Fig. 3A). These visibly older tracks are detectable at the resolution of the elevation model, but field examination showed these deposits to often consist of a single line of individual boulders, where boulders are defined as having a *b* axis greater than 256 mm (Fig. S5). In addition to boulder levees, we also mapped the location of individual boulders/large cobbles (average grain size of 250 mm) found along the

<sup>†</sup>September 2011 storm survey site.

floor of the crater (black dots, Fig. 3A). The large grains were found to go down to elevations as low as 1563 m (the crater floor is located at  $\sim$ 1561 m), which is  $\sim$ 7 m below the highest mapped lake sediments (i.e., Silica Hill) on the crater floor (Kring, 2007).

In Figures 3A and 3B, we show our geomorphic map, as well as a slope map generated from LiDAR data. Slopes steeper than  $\sim$ 32° are either in bedrock or lining the channels cutting through the talus, while the talus itself lies almost entirely on slopes between 20° and 32°. The debris-flow levees crisscross slopes down to  $\sim$ 5°–8°, with localized boulder snouts sometimes found stopped in the tracks of previous leveed debris flows (as was the case for gully 0). The boulder snouts typically were deposited on slopes above 8°, and most are concentrated between 8° and 15°. We note the apparent similarity in elevation

of many of the debris-flow boulder snouts at the lower end of the debris-flow domain, which is  $\sim 5-10$  m in elevation above the highest mapped lake level (dark blue line, Fig. 3A). The lowest-elevation boulders we mapped were found on slopes of  $2^{\circ}-5^{\circ}$ ; if they came down as debris flows, the fine-grained matrix has likely been removed by eolian erosion. Fluvial channels extend past the lobate snout and levee deposits onto slopes less than  $\sim 5^{\circ}$ , and some of them extend all the way to the center of the crater (slopes  $<2^{\circ}$ ).

## **Current-Day Fluvial Processes at Meteor Crater**

In mid-September 2011, a moderate-sized storm occurred in the region near Meteor Crater. The exact amount and intensity-duration patterns

of precipitation that produced runoff inside the crater are not known, as it is not gauged around its rim. However, we do have daily precipitation data from the nearby NOAA Meteor Crater station (35.036°N, 111.023°W). Here, a maximum of 22 mm fell over 24 h, and 85 mm in total fell over 10 d (Fig. 7A). The nearby Winslow airport ( $\sim$ 35 km to the east of Meteor Crater) has a daily average rainfall record for the past 109 yr, as well as the daily record maximums, which have been as high as  $\sim$ 100 mm. After the storm ( $\sim$ 1 wk after final precipitation event), we observed small channels that had incised into gully floors, vegetation that had been flattened in the downslope direction, and small gravel patches that appeared to be recently mobile. Rilling and sheetwash were evident across the gully floors of Meteor Crater, as well as on the outer crater rim. For the gully system we surveyed (i.e., gully 16;

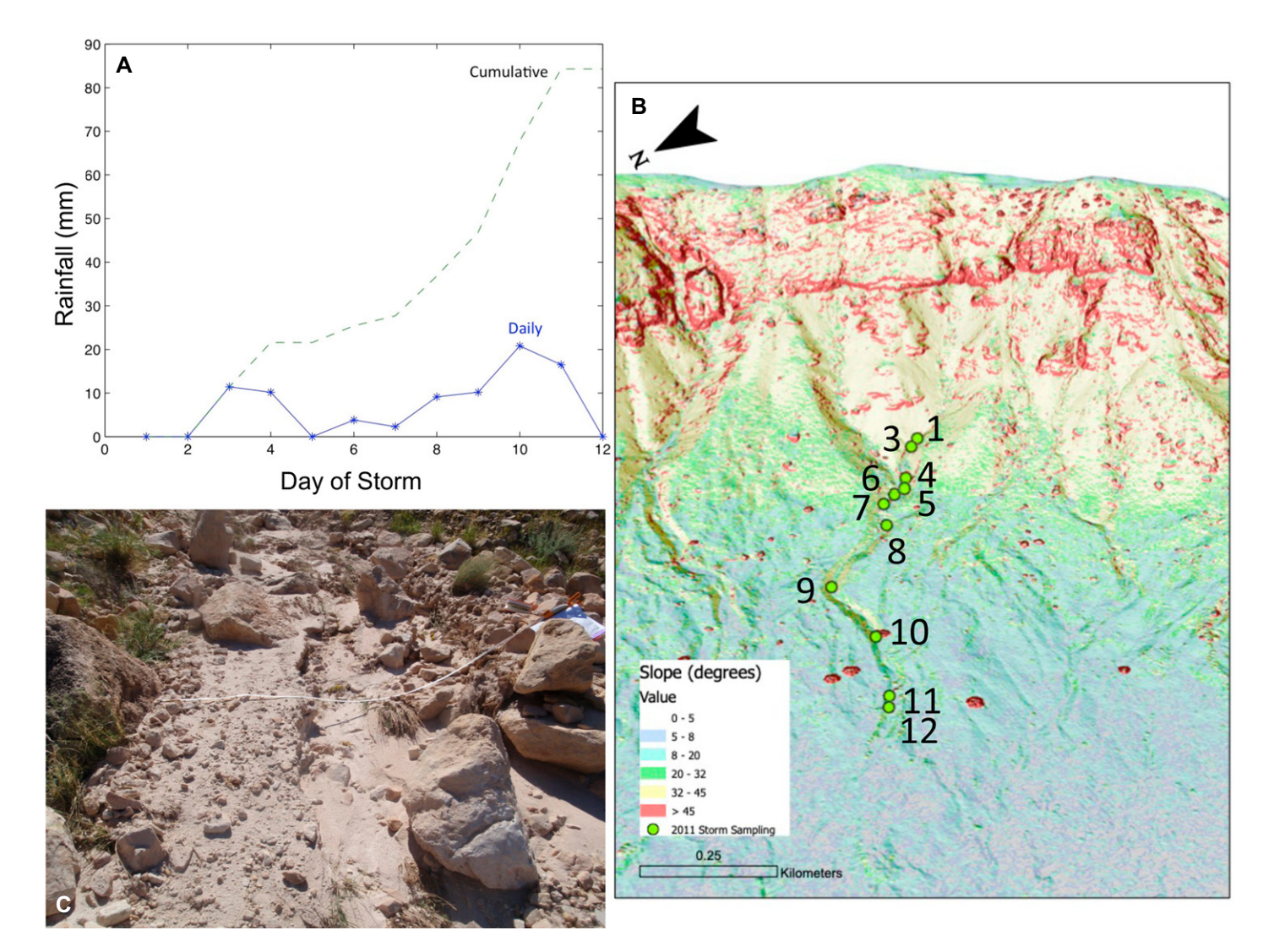


Figure 7. (A) Precipitation data from the National Oceanic and Atmospheric Administration (NOAA) Meteor Crater gauge for the September 2011 storm. Cumulative rainfall amount was ~85 mm, while the maximum daily rainfall was ~22 mm. (B) Sampling locations within gully 16 after 2011 storm event. (C) Fluvial erosion that occurred near site 10.

TABLE 3, DEPTHS, AREAS, AND VOLUMES OF FEATURES AND DEPOSITS WITHIN METEOR CRATER, ARIZONA

Feature/unit	Surface Source area (km²)		Depth (average) (m)	Source	Volume (m³)	Source	Notes		
<u>Depositional</u> Breccia	N.D.	N.D.	175	Shaft data; Kring (2007)	N.D.	N.D.	Deposited immediately postimpact		
Pleistocene lake	0.15	1570 m contour (Silica Hills deposit)	20	Merrill (1908); Hager (1953)	3.0E + 06	Calculated	Highest level of lake sediments observed in Silica Hills		
Pleistocene alluvium	0.34	Shoemaker (1960); geologic map	20	Shoemaker (1960); cross section	6.8E + 06	Calculated	6.0E + 06 m³ estimated to be debris-flow deposits		
Pleistocene talus	0.23	Shoemaker (1960); geologic map	15	Shoemaker (1960); cross section	3.5E + 06	Calculated	debits-flow deposits		
Holocene alluvium	0.21	Shoemaker (1960); geologic map	1.8	Shoemaker (1987)	3.8E + 05	Calculated			
Holocene playa	0.026	Shoemaker (1960); geologic map	1.8	Shoemaker (1987)	4.7E + 04	Calculated	Sediments are composed of pink eolian silt that blows in from outside the crater		
Meteoritic material	N.D.	N.D.	N.D.	N.D.	1.0E + 04	Rinehart (1958)	Within alluvium, lag, and colluvium		
Erosional Gully erosion	0.2	This study	3	This study	8.6E + 05	This study			
Bedrock walls	0.35	Shoemaker (1960); geologic map	9.3	Based on erosion rates from Nishiizumi et al. (1991)	3.2E + 06	Calculated			
		3 <u>3</u> ap		N.D.	5.3E + 06	Calculated	Corrected for changes in porosity to compare with talus/deposits		
N.D.	N.D.	N.D.	N.D.	Shoemaker and Kieffer (1974)	7.0E + 06	Calculated			
				N.D.	1.2E + 07	Calculated	Corrected for changes in porosity to compare with talus/deposits		

Note: N.D.-no data.

survey locations shown in Fig. 7B), the upslope drainage area at the top of the gully (where the incised talus encounters exposed bedrock) is 3867 m<sup>2</sup>, and the main gully channel is on average  $\sim$ 8 m wide and  $\sim$ 200 m long. There was no clear pattern in changes to the fluvial channel depth going downslope, but the fluvial channel width increased from  $\sim 0.4$  m (slopes of  $\sim 25^{\circ}$ ) to 1 m (slopes of  $\sim 5^{\circ}$ ). It was also clear that the fluvial channel path was greatly affected by the vegetation and microscale topography on the gully floor, as it often flowed around vegetated mounds and larger rocks and occasionally would become braided for short distances. At each survey location, there was no evidence for any rilling within the finer-grained material comprising the levee walls, suggesting that the source of water for forming the fluvial channels, like the gullies themselves, was runoff from the exposed bedrock slopes above the gully (i.e., via Horton overland flow).

### ANALYSIS

## Timing, Frequency, and Magnitude of Debris-Flow Events

Samples from debris-flow levees were collected for CRN dating from several of the best-preserved (and presumably most recent) mass-flow events within the crater. The exposure age obtained on the stratigraphically older flow (sample MC-11-01), based on crosscutting relationships, was found to be  $13,910 \pm 670$  yr (late

Pleistocene; Table 1). The exposure ages taken from the stratigraphically younger flow (MC-11-02 and MC-11-03) were  $18,600\pm1230$  yr (late Pleistocene) and  $10,050\pm380$  yr (early Holocene), respectively (Table 1). The oldest exposure age, which was found in the younger flow levee, is suggestive that the boulder we dated was exposed at the surface prior to its entrainment and transport within this flow event.

Assuming debris-flow activity ended by the late Pleistocene to early Holocene, we estimated the average frequency of debris-flow events at Meteor Crater by taking the total volume of material deposited by debris-flow activity and dividing it by the average volume of a debrisflow event (based on the size of surficial deposits) and the time over which debris flows were active within the crater. This assumes one flow event occurs at a time within the crater, but it is possible multiple gullies could be activated at once; our estimate is thus the highest expected frequency. From our geomorphic mapping and slope map (Fig. 3), we assumed that any material deposited between the lowest elevation where debris-flow levees were observed on the crater floor ( $\sim$ 5°), which generally coincides with the elevation of the highest mapped lake deposits, and the transition to talus (20°) was from debris flows. Material deposited below  $\sim 5^{\circ}$  (except for the large, isolated boulders on the crater floor) was assumed to have been emplaced via fluvial processes (and therefore was not included in our estimate). We calculated that there is  $\sim 6.0 \times 10^6$ m3 of debris flow-derived sediment stored on the crater floor (Table 3), which would equate to  $\sim \! 30,\!000$  debris-flow events, assuming the average event size is  $\sim \! 200$  m³ (as discussed above). Based on our CRN dating, we assumed that debris-flow activity was active from the time of impact to the late Pleistocene, which is  $\sim \! 40,\!000$  yr. This equates to  $\sim \! 1$  debris-flow event every 1.5 yr (i.e.,  $6.0 \times 10^6$  m³ debris flow-derived sediment  $\div 200$  m³ per debris-flow event  $\div 40,\!000$  yr with  $\sim \! 0.75$  events/yr or 1 event every 1.5 yr) at Meteor Crater.

# Timing, Frequency, and Magnitude of Fluvial Events

Based on our field data from the September 2011 storm event at Meteor Crater (Table 4), we estimated that the instantaneous water discharge increased from ~0.03 m<sup>3</sup>/s near the head of gully 16 to  $\sim 0.12$  m<sup>3</sup>/s near the floor of the crater. This corresponds to peak runoff rates of  $\sim$ 16–21 mm/h down to  $\sim$ 6–10 mm/h (average  $\sim$ 14 mm/h). Due to the small size of the gully, its steepness, and the relatively impermeable bedrock over which water concentrates, we assumed minor losses to infiltration and evaporation and that the time of concentration is much less than the storm duration (<60 min). As such, we assumed that the system reaches a steady state and that we can directly compare rainfall rates to runoff rates. Based on IDF curves for the region (NOAA, 2011), storms capable of delivering 14 mm of rain in 1 h occur approximately every 1-2 yr, and storms capable

	<u>~</u>		,	~ N	4	œ	4	0	œ	4	_	4	7	_	+		~· ~	.	
	(m³/h)		3	0.32	0.7	1.4	0.2	2.8	0.	2.7	0.	0.7	0.4	7	<u>.</u>		o c	ב <u>י</u>	
	(m³/m/s)		0000	0.00022	0.00034	0.00075	0.0000	0.00114	0.00007	0.00084	0.00003	0.00004	0.00012		0.00008	;	o c	2	al; W* <sub>tot</sub> —
	₩ to(_)		0	0.03	0.10	0.16	0.03	0.20	0.02	0.34	0.04	90.0	0.09	6	0.02		o c	2	r—critica 1 (2015)
	tau*/tau* <sub>cr</sub> (-)		C T	<u>5 5</u>	4.1	1.5	1.2	1.6	1.2	1.8	1.2	1.3	4.	*	-		o c	ž	grains are smaller; H—depth; Q—storm discharge; tau—shear stress (asterisk indicates non-dimensional value); cr—critical; W*or—sport rate: N.D—no data. Prancevic model is from Prancevic et al. (2014). Schneider model is from Schneider et al. (2015).
	eider Jel	tau* (-)	100	0.39	0.31	0.33	0.27	0.32	0.27	0.23	0.18	0.18	0.20	6	0.2.0		o c z z		dimensio from Sc
	Schneider model	tau* (-)	97.0	0.40	0.43	0.51	0.32	0.51	0.31	0.45	0.22	0.23	0.28	2	0.24		o c		tes non-c
ES	Runoff	(mm/h)	1	16.3	21.1	10.9	12.1	16.0	12.9	17.2	8.4	7.1	10.9	0	329.1		512.8 9.2	3.6	erisk indica Schneider
F ESTIMAT	Q storm (m³/s)		000	0.034	0.050	0.052	090.0	0.084	0.00	0.118	0.067	0.063	0.109	0	0.980		0.350	0.000	r stress (ast et al. (2014)
ND RUNOF	Velocity (m/s)		1	1.32	1.38	1.46	1.14	1.54	1.33	1.64	1.0	1.1	1.41	7	 40.		68.0 0.0	50.0	; tau—shea Prancevic
<b>TERS AN</b>	H/D <sub>84</sub>		7	1.20	1.63	1.56	1.40	1.52	1.63	2.35	2,	2.38	2.57	7	7/1		0.86	2	ischarge
PARAME	D <sub>84</sub> (mm)		1	54	37	42	20	23	46	34	59	52	27	1	0.78		65.0 65.0	2.5	–storm d
ANNEL	D <sub>50</sub> (mm)		ü	88	2	55	22	22	27	17	12	4	17	Ċ	00			5	epth; Q-
TABLE 4. CHANNEL PARAMETERS AND RUNOFF ESTIMATES	Hydraulic radius	Œ	2	0.03	0.05	0.05	90.0	90.0	90.0	0.07	0.05	0.05	90.0	7			0.0	0.0	maller; <i>H</i> —d N D —no dat
L	Width/ depth	Œ)	c	၀ ဖ	0	ω	F	6	თ	Ξ	18	16	16	3	/7		125	5	ains are s
	Width (m)		9	0.4	9.0	0.55	0.75	0.68	0.7	6.0	<del>-</del> -	0.95	Ţ.	•	4		<b>^</b> ^		of the gr
	Depth (m)		9	0.065	90.0	0.065	0.02	0.08	0.075	0.08	90.0	90.0	0.0	Ļ	0.10		0.056	0.00	which 84%
	Slope (-)		2	0.475	0.3	0.35	0.225	0.325	0.225	0.175	0.1	0.1	0.125		5		0.36	20.0	in size at V—bed-ld
	Bedrock drainage	area (m²)	Jully 52)	, Z O.Z	N.D.	N.D.	N.D.	N.D.	N.D.	N.D.	N.D.	N.D.	N.D.	7	4/00	ow initiation	o c		ize; $D_{\rm st}$ —grai
	Drainage area from	sample site (m²)	직	7575	8450	17,225	17,800	18,775	19,400	24,650	28,675	31,900	35,775	<u>shannel</u>	10,783	el for debris-flo	2460	2400	Note: $D_{so}$ —median grain size; $D_{sa}$ —grain size at which 84% of the ndimensional bed-load transport rate: W—bed-load (sediment) tran
	Site number		September 2011	- ო	4	2	9	7	8	6	우	=	12	Pre-May 2011 channel	Gully 6/	Prancevic model for debris-flow initiation			Note: D <sub>so</sub> —median grain size; D <sub>so</sub> —grain size at which 84% of the grains are smaller; H—depth; Q—storm discharge; tau—shear stress (asterisk indicates non-dimensional value); cr nondimensional bed-load transport rate: W—hed-load (sediment) transport rate: N D—no data Prancevic model is from Prancevic et al. (2014). Schneider model is from Schneider et al.

of delivering 21 mm of rain in 1 h occur every 2-5 yr. If infiltration and evaporation reduce runoff by 50% (such that  $\sim$ 28 mm of rain is required to get an average of  $\sim$ 14 mm of runoff), storms of this magnitude occur approximately every 10 yr. To estimate the volume of sediment transported in a yearly to decadal storm event at Meteor Crater, we compared the nondimensional bed shear stresses during the storm  $(\tau^*)$  to the critical Shields stress ( $\tau^*_{cr}$ ), i.e., the threshold at which sediment begins to move. When the ratio  $\tau^*/\tau^*_{cr} > 1$ , sediment transport theoretically occurs. Using the Schneider et al. (2015) model, we found that  $\tau^*/\tau^*_{cr}$  ranged from 1.2 to 1.8 at all sites, which translates to sediment fluxes between 0.1 and 2.8 m<sup>3</sup>/h (average  $\sim$ 0.9 m<sup>3</sup>/h). If similar transport rates occurred in every gully around the crater, then a storm event of this magnitude would transport  $\sim$ 66 m<sup>3</sup>/h of sediment. Assuming all the Holocene alluvium deposited on the crater floor (Table 3) is fluvial in origin (as it has been deposited on slopes  $<5^{\circ}$ ), then  $\sim$ 5700 transport events likely occurred over the last  $\sim$ 10,000 yr (or 1 event every 2 yr on average). Larger fluvial runoff events have occurred at Meteor Crater, based on the 4-m-wide fluvial channel observed in gully 0 that formed prior to the September 2011 storm event.

### **Sediment and Water Budget**

Our field observations and CRN dating results suggest that debris-flow activity was mostly confined to the Pleistocene (with events as often as every 1 to 2 yr), whereas in the Holocene, most sediment has likely been transported via fluvial events. In terms of a sediment budget, the sediment available for transport within Meteor Crater is largely postimpact material (i.e., the breccia lens and postimpact talus) and debris from erosion of the rim (see fig. 6.4 in Kring, 2007). Nishiizumi et al. (1991) estimated rim retreat rates of  $\sim$ 9 m on the west side of the crater using CRN (i.e., 30 cm/1000 yr for the first  $\sim$ 27,000 yr and 5 cm/1000 yr in the last ~23,000 yr), while Shoemaker and Kieffer (1974) estimated  $\sim$ 12 m of erosion on the NE crater flank, which they assumed was a minimum number, and so they estimated that closer to a total of 15-20 m of erosion has occurred. Taking this range of estimates into account and applying them to the inner crater bedrock wall area ( $\sim 0.35 \text{ km}^2$ ) results in  $\sim 5.3 \times 10^6 \text{ to}$  $1.2 \times 10^7 \, \text{m}^3$  of sediment delivered to the crater walls and floors (Table 3). Based on our estimates of the volume of material deposited on the crater floor as lake sediment ( $\sim 3 \times 10^6 \text{ m}^3$ ) and Pleistocene alluvium ( $\sim 6.8 \times 10^6 \text{ m}^3$ ), and assuming negligible material has been blown in from outside the crater, this would argue for rim

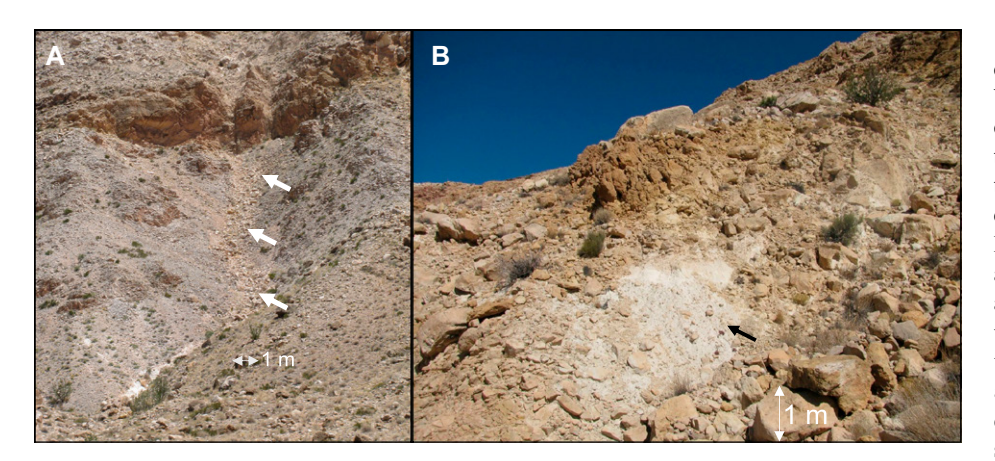


Figure 8. (A) Debris from upslope rockfall filling the floor of a large gully located on the southern wall of the crater. (B) White fine-grained material supporting a coarser gravel layer within the wall of gully 0.

erosion rates closer to those suggested by Shoemaker and Kieffer (1974), or considerable erosion into the impact-generated breccia and talus. However, we calculated that the volume of material removed from areas mapped by Shoemaker (1960) as Pleistocene talus to form the gullies we observe today is  $\sim 8.6 \times 10^5$  m<sup>3</sup>. This accounts for only  $\sim 13\%$  of the material mapped as Pleistocene alluvium by Shoemaker (1960), which we suggest has been emplaced by mostly debrisflow processes on the crater floor, and only  $\sim 9\%$ of the total sediment on the crater floor. This suggests that once formed, these gullies have repeatedly been filled with sediment from rockfall and erosion of the upslope bedrock and then scoured by debris-flow and fluvial events. Evidence of this infilling process is observed today, where we observed  $\sim$ 1 m of infill in the gully channel in several gullies on the eastern wall (Fig. 8A).

Similar to calculations done on Mars (e.g., de Haas et al., 2015a), we can use our volumes of fluvial- and debris flow-deposited sediment on the lower crater slopes and crater floor to estimate minimum water amounts that were needed to transport these sediments (i.e., not accounting for infiltration and evaporation). We first determined the minimum amount of water needed to transport sediment as a debris-flow event for comparison with modern precipitation inputs to see if drier conditions in the Holocene can explain the lack of mass-flow events. We took our estimate of the volume of sediment within the terminal snout and levees at gully 0 (283 m<sup>3</sup>) and then assumed a rock-to-water ratio (by volume) of 0.3 based on experimental work by Kaitna et al. (2016), who showed that this ratio is the transition from debris-flow to fluvial behavior. This requires at least 85 m3 of water to initiate and transport sediment from the crater wall to the floor (assuming no losses to infiltration and

evaporation). The water source area for gully 0 is ~4700 m<sup>2</sup>, which equates to 18 mm of runoff to generate a flow. If we use a rock-to-water ratio of 0.3 and apply it to the entire volume of debris-flow deposits on the crater floor, then it would have taken a total of  ${\sim}2\times10^6\,\text{m}^3$  of water to transport the observed sediment, or  $\sim$ 6 m of runoff (for a bedrock area of 0.35 km<sup>2</sup>). Using rainfall data from the Winslow Airport (Arizona) (wrcc.dri.edu), a total of almost 20 m of rainfall has fallen over the past 109 yr of record, and daily records show that moderate storms at the crater routinely deliver >18 mm of precipitation. This would suggest that even under Holocene climate, enough total water for debrisflow transport has been delivered to the crater. However, over the past 100 yr at the crater, there have been no observed debris-flow events, except for a small mudslide near the man-made trail on the northwestern rim in 1906 (Fairchild, 1907; Kring, 2007). Furthermore, our CRN ages of the youngest boulders and those reported by Nishiizumi et al. (1991) date to the late Pleistocene or early Holocene. This implies that (1) much more water than just that needed to fill the pore space of a pile of sediment is needed for debris flows to occur at Meteor Crater and (2) the rate of water delivery and ability to generate runoff need to be considered. IDF curves for the region (NOAA, 2011) suggest that rainfall can be delivered relatively rapidly, with  $\sim$ 18 mm of rainfall falling in under 30 min at a frequency of every 5-10 yr. If infiltration and evaporation use 50% of the water needed for initiation (such that a total of 36 mm of rain is required to get 18 mm of runoff), storms of this intensity lasting <30 min occur every 50-75 yr. Either much higher intensities are needed than can be achieved by the current climate, or the ability to generate sufficient runoff has declined (as will be discussed below).

In terms of sediment delivery by fluvial processes, we can also take a rock-to-water approach. We first assumed that most of the sediment deposited within the Pleistocene-aged lake was transported fluvially (though we acknowledge that some fraction may have been blown into the crater, similar to the modern-day playa deposits). If we take our estimated volume of lake sediment and use a rock-to-water ratio of 0.0002 (based on a survey of desert rivers by Pepin et al., 2010), it would have required ~15 km<sup>3</sup> of water to transport the observed sediment, or  $\sim$ 13.6 km of runoff (for a crater area of 1.1 km2). Applying modern precipitation rates (~20 m per 109 yr) over the possible duration of the lake during the Pleistocene ( $\sim$ 40,000 yr), this would equate to only  $\sim$ 7 km of runoff, or half of the water needed. This would imply that during the Pleistocene, the Meteor Crater region would have been at least  $\sim 2 \times$  wetter to transport all the crater lake sediments.

#### DISCUSSION

### Controls on Debris-Flow and Fluvial Processes at Meteor Crater

A key motivation for investigating the deposits and erosional features at Meteor Crater was to quantify the role of fluvial versus debris-flow processes in the crater's evolution, and how (and whether) the occurrence and frequency of these processes are functions of climate change. As discussed above, prior work by Kumar et al. (2010), following Shoemaker and Kieffer (1974) and Grant (1999), suggested that postimpact, fluvial processes from seepage eroded the crater wall and subsequently deposited the material now mapped as Pleistocene talus. They hypothesized that further incision of the talus was due to a later period of enhanced erosion, perhaps via rainfall, and pointed to their mapping of a branched network of channels that originate on talus (see fig. 7 in Shoemaker and Kieffer, 1974) as evidence for this second erosion event. We propose an alternative erosion history, where postimpact (immediately after which there was breccia and talus emplacement) runoff over upslope bare bedrock (from rainfall or snowmelt) entrained sediment and incised the gullies predominately via debrisflow processes. Based on our field and LiDAR mapping, the branched network of channels on the talus interpreted by Kumar et al. (2010) to be fluvial in origin is instead from debris-flow tracks that formed as debris flows were deposited/terminated (and fluvial channels form within these tracks and can transport sediment further out onto the crater floor). Debris flows are self-bounding, such that they create levees as coarse debris is advected laterally (e.g., Whipple and Dunne, 1992), and net accumulation of sediment occurs as successive flows cross and switch canyons (Fig. 5). As such, a second period of enhanced precipitation is not necessarily required in our model. When water inputs are not sufficient to generate a debris flow at Meteor Crater, as was observed during the September 2011 event, fluvial activity, also driven by overland flow processes, leads to minor modification of the gully floor and the transport of finer sediment within the debris-flow tracks. CRN dating of the visually youngest pairs of debris-flow levees in the crater suggests that debris-flow activity occurred mostly in the Pleistocene, while the Holocene has seen mainly fluvial activity. We discuss the possible sources and roles of water, sediment supply, and crater evolution on controlling this process transition in the following.

Both debris-flow and fluvial processes, then, appear to be driven by surface runoff, where water is concentrated on the exposed bedrock walls during storms (or perhaps snowmelt events in the past) and is delivered to the talus slopes below. However, due to the highly fractured nature of the Kaibab plateau surrounding Meteor Crater (Kumar and Kring, 2008), fractures may act as conduits for transferring water from the surface to the subsurface. Huntoon (2000) showed that these fractures are so efficient at dewatering the Kaibab plateau in the vicinity of the Grand Canyon that there are no perennial streams in that region. It is therefore possible that a secondary source of water into the crater (after Horton overland flow) is from infiltrated surface water (Kumar et al., 2010). However, while water can rapidly drain downward through joints in the Moenkopi and Kaibab Formations, when it hits the less permeable Toroweap Formation, it will likely flow radially away from the crater, as the Toroweap surface is uplifted and tilted back from the crater wall. Also, the lack of staining and/or gravel lag at the head of each gully and the fact that erosion from seepage has only ever been validated in cohesionless sediment (Howard and McLane, 1988; Schumm et al., 1995), or very weakly cemented sandstones (Lamb et al., 2006), support the interpretation that this is likely not the primary source of water leading to gully formation.

In regard to the amount of runoff delivered to Meteor Crater, our simple water and sediment budget suggests that perhaps twice as much runoff was needed in the Pleistocene (compared to contemporary amounts) to deliver fine sediment from the crater walls into the lake. Furthermore, sufficient runoff and/or groundwater inputs would have been needed to support a sustained lake. For sediment delivery by mass flows, however, the rock-to-water approach, which is commonly used on Mars, would suggest relatively little water is needed and that modern-day

precipitation and runoff are sufficient to trigger debris flows. This method only considers the total volume of water entrained within a debris flow, however, and it does not consider the rainfall-runoff conditions needed to initiate a flow. Other mass-flow events observed in this region typically initiate under high-intensity rainfall that occurs over 15 to 30 min intervals (Staley et al., 2020). Unfortunately, paleoenvironmental data from the late Pleistocene and early Holocene in the region cannot constrain precipitation or runoff rates, especially shortduration, high-intensity events, but evidence generally points to a cooler, wetter period, with precipitation amounts being ~120% to 150% greater than current day (Cole et al., 2013). At a broader spatial scale, modeling by Matsubara and Howard (2009) for the western United States showed that runoff depths in the late Pleistocene would have ranged  $\sim 1.7$ –4.1× modern values to reproduce paleolake basin distributions (e.g., Lakes Bonneville, Lahontan, and Manly). It is not clear, however, whether the cooler and wetter climate from the late Pleistocene would have had more frequent high-intensity rainfall events than the current climate, which is dry but subject to monsoons. While more monitoring and modeling are needed to determine the rainfall intensities that generate runoff at Meteor Crater, there is value in understanding the possible mechanisms by which mass flows initiate within the crater, as it provides clues on why debris flows ceased  $\sim$ 10,000 yr ago.

## Mechanisms of Debris-Flow Initiation Processes

Here, we discuss in more detail several mechanisms proposed at other study sites for how concentrated runoff can lead to debris-flow initiation, downslope entrainment, and deposition.

One mechanism proposes failure of a fluvial channel bed by surface runoff. Takahashi (1978) put forth a quantitative model that assumes that failure of a sediment bed with slope-parallel seepage occurs when surface runoff exerts stresses that can exceed the resistance of the granular bed. In addition, if the bed failure depth is equal to or greater than 0.5 times the flow depth, then sediment can disperse uniformly through the flow and move as a debris flow. Prancevic et al. (2014) recast the Takahashi (1978) model in terms of critical Shields stress for debris-flow initiation ( $\tau^*_{c,df}$ ):

$$\tau_{c,df}^* = \frac{\rho hS}{\left(\rho_s - \rho\right)D_{50}} = \left(1 - \eta\right)(\tan \varphi - S)$$
$$-\frac{\rho}{\rho_s - \rho}S,\tag{8}$$

where  $\eta$  is porosity, and  $\varphi$  is the internal friction angle of the sediment. For the range of slopes (S) where debris-flow entrainment likely occurred at Meteor Crater,  $\sim 20^{\circ}$  to  $\sim 32^{\circ}$ , the experimental results from Prancevic et al. (2014) suggest that the critical Shields stress for debris-flow initiation would range from 0.4 down to 0.12 (for  $\phi = 55^{\circ}$ ), respectively. Rearranging Equation 8 and using a  $D_{50}$  of 31 mm (based on our pebble count of the gully floor in gully 16 near site 1), we calculated that the runoff depth needed to cause failure of the bed is  $h \sim 10-57$  mm. We used Equations 2 and 3 to estimate mean velocity, but as the Ferguson (2007) formulation (Eq. 3) has only been validated up to slopes of  $\sim 20^{\circ}$ , and fluvial channels were not observed at 32°, if we take our runoff depth estimate of 56 mm (for a slope of 20°), we find a flow velocity of 0.8 m/s and a discharge of 0.02 m<sup>3</sup>/s (for a 0.5-m-wide fluvial channel). For a crater average upslope bedrock area of 2460 m<sup>2</sup>, this equates to a runoff rate of  $\sim$ 33 mm/h (though this does not account for the water load needed to saturate the gully bed material). While the Takahashi (1978) and Prancevic et al. (2014) model has not been tested on slopes as steep as those at Meteor Crater (i.e.,  $> 20^{\circ}$ ), or with such coarse grain sizes, it does illustrate that while the body of a debris flow contains relatively little water for its sediment load, appreciable amounts of water (both surface runoff and subsurface flow) might be required for debris-flow initiation.

While the Takahashi (1978) model proposes that debris flows can form within fluvial channels under relatively steady flow conditions, others have proposed that debris flows initiate in a more chaotic fashion, often termed the "firehose effect." In this model, sediment is mobilized when a concentrated flow of water (normally from intense rainfall over steep bedrock channels) hits unconsolidated sediment, such as debris dams that form in steep channels or talus material at the base of bedrock slopes (e.g., Johnson and Rodine, 1984; Berti et al., 1999; Berti and Simoni, 2005; Coe et al., 2008; Gregoretti and Fontana, 2008). The amount of water needed to initiate debris flows by this mechanism has not been well quantified. Field observations suggest that some amount of water is needed to saturate the sediment/talus prior to its entrainment (e.g., Curry, 1966), but the common assumption of steady, uniform flow for determining shear stress is likely not appropriate, as observations suggest the flow is highly nonuniform (e.g., jets; Costa, 1984; Berti et al., 1999; Cannon et al., 2003; Kean et al., 2013), and part of the sediment entrainment process is likely due to the force of the fluid momentum and the fact that the rapid delivery of water outpaces infiltration. Looking at other modern-day debris-flow events sug-

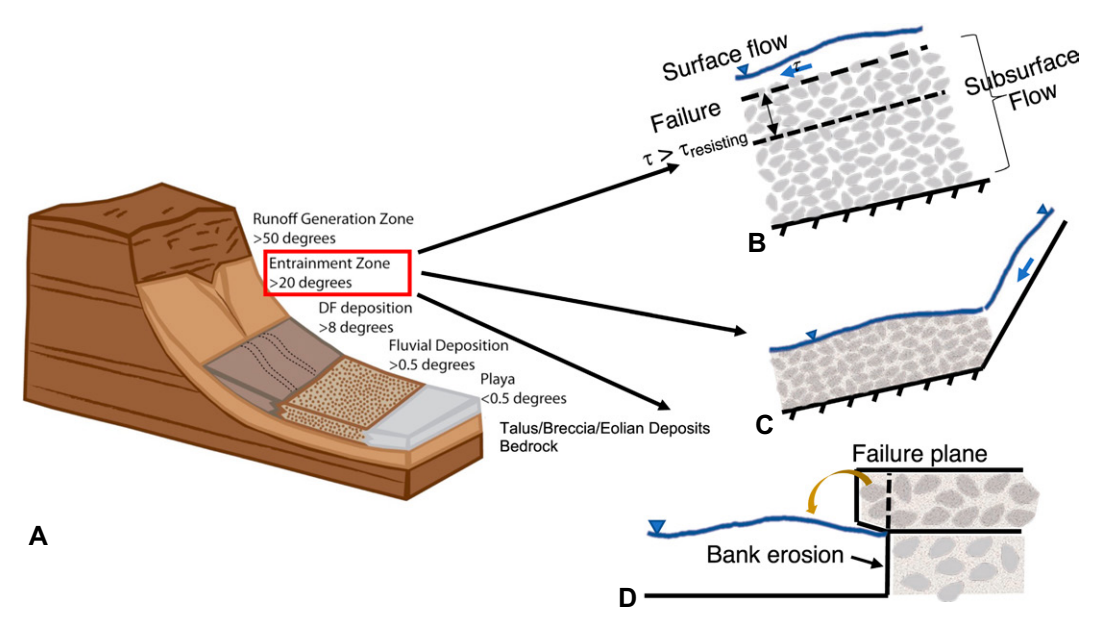


Figure 9. (A) Conceptual model for gully formation. (B) Entrainment into a debris flow (DF) can result from surface runoff that leads to shear entrainment of the sediment bed. (C) "Fire-hose" effect, which requires rapid delivery of water from the upper crater bedrock walls to the talus below. (D) Alternatively, fluvial runoff may undermine the channel floor and adjacent banks, which collapse onto the flow and transform it into a debris flow.

gested to be initiated in this way in the western United States, Godt and Coe (2007) found that debris flows were triggered in talus in response to a thunderstorm that produced ~43 mm in 4 h, most of which fell in the first 2 h, while McCoy et al. (2010) found that a short-duration (<3 h) rainstorm with low- to moderate-intensity rainfall (<10 mm/h) triggered debris flows in Chalk Cliffs, Colorado. Regional IDF curves suggest that similar short-duration and high-intensity storms occur at Meteor Crater at approximately decadal to 50 yr frequencies, but the grain-size distribution and talus properties likely matter when predicting the hydrologic conditions under which they will be entrained and mobilized.

For example, fine-grained sediment (i.e., clayand silt-sized material) is often cited as a necessary ingredient for producing debris flows (e.g., Major and Pierson, 1992; Griffiths et al., 1996; Meyer and Well, 1997). The fines are thought to mix with water to form the highly viscous pore fluid that mediates intergranular collisions, prevents separation of the fluid and solid components of the flow, and reduces resistance to flow, enabling transport on gentle slopes (Pierson, 1981; Iverson, 1997; Kaitna et al., 2016). At Meteor Crater, near the gully headwalls, a layer of finer-grained white material supports many of the larger clasts (see Fig. 8B); these fines, perhaps generated during the impact, are likely necessary for causing entrainment into a mass flow. However, winnowing of this material has occurred (both by fluvial processes and wind erosion), as evidenced by rock flour mapped on the crater floor and within borehole sediments (Kring, 2007). Loss of this material over time will both increase the saturated conductivity of the talus, which in boulder-rich talus is set by

the conductivity properties of the fines filling the pore space (Bouwer and Rice, 1984), and decrease the viscosity of the pore fluid, both of which make it more difficult to generate the conditions needed to transport coarse grains as a debris flow (e.g., Kaitna et al., 2016).

A third mechanism for debris-flow formation at Meteor Crater is from collapse of gully walls/banks due to fluvial erosion and undercutting, such that runoff is suddenly charged with a high sediment load and transitions into a debris flow (i.e., bulking; Takahashi, 1978; Gregoretti and Fontana, 2008). Under this model, boundary shear stresses along the wetted perimeter of the gully channel and sidewalls must be sufficient to overcome bank cohesion, where the local boundary shear stress is proportional to the downstream component of the weight of the fluid (which is a function of the hydraulic radius in narrow channels; Nagata et al., 2000). Thus, as gully channels evolve and widen with time due to undercutting and bank failure, it would take higher discharges to maintain the same local boundary shear stresses (due to decreasing flow depths) following conservation of mass (i.e., Eq. 1). It is therefore possible that even if Pleistocene climate conditions persisted, debris-flow activity would have decreased.

As originally suggested by Kumar et al. (2010), Meteor Crater provides a unique environment in which to probe whether there is a direct relationship between erosional processes and climate change. The simplest analysis we performed, using sediment-to-water ratios and deposit volumes, suggests much greater runoff during the Pleistocene. However, this method would also suggest that very little water is needed to transport sediment via debris-flow

processes, so even modern-day runoffs would be sufficient. As discussed above, the ways in which debris flows initiate also matter to the water budget (Fig. 9). Fluid shear entrainment of the crater talus and gully floors likely requires large volumes of water to both saturate the sediment on the gully floors and generate sufficient overland flow ( $\sim$ 1–5 cm on steep slopes with small drainage areas) to cause bed failure. It is possible that if this mechanism dominated at Meteor Crater, then the climate transition from the Pleistocene to the Holocene was the main driver in debrisflow cessation. The second mechanism is the "fire-hose" effect, which also requires rapid delivery of water from the upper bedrock walls of the crater to the talus below (i.e., a wetter climate), and enough fine-grained sediment to generate interstitial fluid capable of mobilizing the coarser talus grains. Debris flows suggested to have initiated by this mechanism in the southwestern United States did so under storm conditions that currently occur at Meteor Crater (based on IDF curves), suggesting that winnowing of fines from the talus over time (by wind or fluvial erosion) might also play a key role in the transition from debris flow-dominated to more fluvial-dominated activity at the crater. Last, the growth and evolution of the gullies themselves might lead to a shift in process; if sediment bulking from bank collapse is a potential debris-flow trigger, then widening of the gullies over time would require greater discharge to generate the shear stresses capable of scouring the gully walls and floor and causing bank failure. In this scenario, even if climate change does not occur. debris-flow activity may ultimately diminish due to gully evolution. Of course, all these mechanisms might have occurred at different times in the evolution of the crater walls. This points to the importance of climate in the rate and type of erosional processes acting on the crater wall at Meteor Crater, but also the importance of environmental factors, such as grain-size distribution, sediment supply, and gully morphology, which might lead to spatially variable responses across the crater for a given storm event.

# Conceptual Model for Gully Formation in Talus in Steep Bedrock Landscapes

Our topographic analysis of Meteor Crater suggests a general morphodynamic model for gully incision into talus and subsequent deposition by debris-flow and fluvial processes. Examples of environments where large talus deposits develop at the base of steep bedrock slopes, besides impact craters, are below cirque heads and sidewalls after glacier retreat (e.g., in the Colorado Rocky Mountains; Caine, 1986; Godt and Coe, 2007), in periglacial basins affected by frost weathering processes (Hales and Roering, 2007; Palucis et al., 2023), and steep postfire landscapes (e.g., San Gabriel Mountains; Lamb et al., 2011). Generally, three primary process zones can be identified: a runoff generation zone (typically off bedrock), a sediment entrainment zone (a bedrock slope mantled with colluvium, impact breccia [in the case of a crater], and/or eolian deposits), and a depositional zone (Fig. 9). Empirical studies elsewhere, as well as at Meteor Crater, suggest that each of these zones can be distinguished by characteristic slopes (Fig. 3B), in which the water source region tends to be steeper than 32°, the entrainment zone extends from  $\sim 32^{\circ}$  to  $\sim 20^{\circ}$ , and the deposition zone progressively declines from debris flow-dominated (down to about  $\sim 8^{\circ}-5^{\circ}$ ) to, if present, fluvial (commonly  $<\sim 1^{\circ}$ ) and flat lake sediments.

When runoff (either from snowmelt or rainfall) is generated over impermeable bedrock, it crosses onto a lower, sediment-mantled zone, and entrainment occurs. The mechanism by which sediment is entrained into a debris flow via runoff can vary, but, in general, some combination of sediment entrainment, bed failure, and destabilization of gully walls causes a mixture of colluvium (i.e., boulders, gravel, sand, and mud) to rapidly charge the flow, leading to a debrisflow surge. This sediment-rich mass may continue to entrain colluvium and increase in size until it reaches lower unconfined slopes, where deposition ensues.

Runoff into a gully lacking sufficient duration or intensity to cause entrainment to mass flows may be able to transport finer sediment by fluvial processes. Gully walls and/or the levees left by the debris flows will confine these flows. Flow of sufficient duration may spill past the debrisflow deposits and build a lower-gradient alluvial fan downslope. Hence, both debris-flow and fluvial processes may occur in gullies, depending on the magnitude of runoff. Gully development may also be nonlinear, in that initial incision will focus subsequent runoff, entrainment (if the shear stress exceeds the threshold for sediment transport), and mass failure from the upslope sediment source area. The growing walls driven by gully incision would lead to increased sediment flux to the channel, which could serve to enhance entrainment and incision. Over time, as the gullies widen and slopes decline, runoff events may be unable to cause sufficient bed and bank erosion (due to reduced shear stresses), thereby stabilizing the channel width and forcing the mode of transport to be fluvially dominated.

### **Meteor Crater as a Mars Analog?**

Being an impact crater with well-developed gully features naturally leads to questions about the applicability of Meteor Crater as an analog to understanding gullying on Mars. In some respects, Meteor Crater is very different than documented recent Martian gullied craters because it is much smaller (the gullies identified by Malin and Edgett, 2000, have gully heads that are several hundreds of meters wide, as opposed to tens of meters at Meteor Crater), it is not within a basaltic lithology, erosion is driven by rainfall (possibly rapid snowmelt as well), and the terrain into which Martian gullies are observed to form, which likely contains a large fraction of fine sediment and possibly appreciable ice (e.g., Mustard et al., 2001; Christensen, 2003), is absent.

However, the morphology of the Meteor Crater gullies is remarkably similar to many Martian gullies. Martian gully alcoves are often at the crest or midway down the talus slopes along crater walls, incise into both bedrock and slope deposits, and contain meter-scale boulders (de Haas et al., 2013, 2015a, 2015b; Núñez et al., 2016). Channels can be V-shaped in cross section (Mangold et al., 2010; Hobbs et al., 2013) and contain fluvial features such as terraces and longitudinal bars (Schon and Head, 2009), or they can contain mass-flow features such as levees (Levy et al., 2010; Johnsson et al., 2014; Sinha et al., 2019). At their distal end, Martian gullies often have lateral levees, lobate or digitate ("finger-like") deposits, and/or poorly sorted coarse material. De Haas et al. (2015b) observed sedimentological evidence of debris flows on 51 gully fans across the southern midlatitudes of Mars, where exposures in incised channels contained meter-scale boulders randomly distributed in a finer-grained matrix, with occasional lens-shaped and truncated layering, which are characteristic of the deposits found at Meteor Crater. When Conway and Balme (2016) compared the morphology of Martian gully alcoves (in cumulative/noncumulative area distribution space) to catchments that form from dry granular flows on the Moon and Earth, as well as terrestrial debris flows and fluvial gully catchments, they found that Martian gully source areas are statistically dissimilar to dry granular systems. These observations have led to the general consensus that the majority of gullies on Mars required some fluid or fluidization process to form (Harrison et al., 2015; Conway et al., 2019) and that only very recent flows, often mapped as bright deposits found above angle-of-repose slopes, might be dry in origin (Malin et al., 2006; Kolb et al., 2010).

As current Martian conditions render liquid water highly unstable, constraining gully formation mechanisms and associated fluid volumes and discharges has been a key goal of research into the modern Mars environment for the past two decades. Malin and Edgett (2000) showed that gully heads are often associated with distinct layers within a cliff, which they suggested points to seepage during obliquity-induced freeze-thaw cycles (when ice plugs melt or fracture), but this model (and other variants; e.g., Hartmann et al., 2003; Coleman et al., 2009) requires an unrealistically high-permeability aquifer, a very briny aquifer, or high geothermal fluxes (Goldspiel and Squyres, 2011). Mapping of thousands of gullies across Mars has shown that gullies tend to be located at mid- to high latitudes in both hemispheres and are associated with Martian surface features thought to be related to past and/or present surface ice (e.g., Dickson et al., 2007; Dickson and Head, 2009; Goldspiel and Squyres, 2011; Harrison et al., 2015). As such, some models invoke the melting of near-surface ice, resulting in landsliding or sediment erosion by exfiltration of meltwater (Costard et al., 2002; Gilmore and Phillips, 2002), though the predicted gully morphology is dissimilar to most Martian gullies (Gallagher and Balme, 2011; Conway et al., 2019). A problematic feature for all near-surface ice-melt scenarios is that model results suggest that over the past 5 m.y., the 273 K isotherm has typically been above nearsurface ground ice at the mid- to high latitudes (Mellon and Phillips, 2001). Any melting that does occur would primarily occur during the summer (e.g., de Haas et al., 2015a), but active flow events on Mars have been observed mostly during the fall, winter, or early spring (Harrison et al., 2009; Diniega et al., 2010; Dundas et al., 2015). Carbon dioxide is a major constituent of the modern Martian atmosphere and will condense during the midwinter, leading to CO<sub>2</sub> frost cover from the poles to the midlatitudes  $(\sim 50^{\circ}$ ; Piqueux et al., 2015) and on pole-facing steep slopes between latitudes of 30° and 50° (Vincendon et al., 2010a). There is support for CO<sub>2</sub>-related mechanisms triggering present-day flows, as active gullies are exclusively within the zone of observed or predicted CO<sub>2</sub> ice (Diniega et al., 2010; Dundas et al., 2015; Raack et al., 2015; Pasquon et al., 2016), and it is possible CO<sub>2</sub> frost processes are a significant part of initial gully formation in these regions (Dundas et al., 2022). However, contemporary gully activity has not been observed at latitudes equatorward of where CO2 frost is observed spectroscopically (i.e., 45°S-30°S; Vincendon et al., 2010a, 2010b), so the role of past water cannot be ruled out for all Martian gullies (Dundas et al., 2015). Interestingly, de Haas et al. (2019) showed that for contemporary gully systems, flows triggered by CO<sub>2</sub> result in morphologies similar to those of granular flows on Earth (i.e., like those observed at Meteor Crater). Fluvial models have also been applied to Martian gullies, but they result in large water volumes that are difficult to reconcile with more recent Martian climate (e.g., Parsons and Nimmo, 2010). De Haas et al. (2015a) mapped individual debris-flow events in the young (Johnsson et al., 2014), midlatitude Istok Crater and found that 3-9 mm of liquid water would need to be uniformly spread over individual alcoves  $(\sim 4 \times 10^4 \text{ m}^2 \text{ per alcove})$  to generate modalsize debris-flow events; this is assuming terrestrial debris-flow size-frequency relationships and sediment-water ratios (but as we discussed herein, the water needed to initiate a debris flow event is not accounted for).

Thus, based on their morphology, occurrence of debris-flow and fluvial events, and exposure to a drying climate, the Meteor Crater gullies are relevant to understanding many Martian gullies. Our work highlights several important factors when trying to use geomorphic landforms to assess past hydrologic or climatic conditions on Mars. First, the dominant flow process can change both with climate and surface conditions (e.g., grain-size composition, sediment supply, slope, gully width) such that the modern-day processes we can observe on Mars may only be modifying already existing gullies (e.g., Johnsson et al., 2014). Thus, more work is needed to understand the ranges of conditions and processes that lead to the initial incision of gullies on crater walls, as well as the conditions that "turn off" gully formation. Field sites like Meteor Crater, where we broadly understand its climate history and can use a combination of field mapping, geochronology, and lake core records to obtain better constraints on the linkage between erosion processes and timing and climate, are invaluable to ultimately understanding crater evolu-

tion on Mars. Second, the use of deposits and erosional landforms, at least at Meteor Crater, likely underestimates total water inputs as well as the intensity and duration of those inputs (and the climatic regime those imply). This is an important consideration when doing simple water budget analyses on Mars, like using sediment-to-water ratios that do not account for the additional water required to trigger a debris flow, and inferring paleoclimate conditions (e.g., Mangold et al., 2012; Morgan et al., 2014; Palucis et al., 2014; de Haas et al., 2015a). A better mechanistic understanding of the ways in which sediment is transported on steep slopes, and the associated water volumes and rates, especially under different climate conditions, will aid in our ability to develop more accurate models for Martian systems.

### **CONCLUSIONS**

Since its formation  $\sim$ 50,000 yr ago, Meteor Crater has undergone significant modification as  $\sim$ 71 gully systems incised into its inner walls during the first ~40,000 yr of pre-Holocene wetter conditions. Fieldwork and cosmogenic dating on an individual gully system combined with a detailed topographic analysis of LiDAR data suggest an alternative explanation to the previously proposed seepage erosion and fluvial incision model for the Meteor Crater gullies. We propose that debris-flow processes dominated gully incision, as evidenced by the presence of poorly sorted, matrix-supported levee deposits and coarse-grained lobate deposits with steep lateral margins. These flows were generated predominately by runoff from bare bedrock. When water inputs are not sufficient to generate a debris flow, as was observed during a storm event in September 2011, fluvial processes driven by overland flow processes lead to minor modification of the gully floor. Cosmogenic dating suggests that most of the modification of the walls of Meteor Crater occurred before the early Holocene, which coincides with a lake on the crater floor and other paleoenvironmental factors from the southwestern United States suggesting wetter and cooler conditions. Future study on the timing and evolution of the crater lake, and its influence on gully evolution, will provide further constraints on the evolutionary history of the inner crater walls and floor.

On average, debris-flow events at Meteor Crater consisted of  $\sim 200~\text{m}^3$  of material. To account for the total volume of debris-flow deposits currently deposited on the crater floor, debris-flow frequency was  $\sim 1$  event every 1.5 yr, assuming debris-flow activity terminated  $\sim 10,000~\text{yr}$  ago. Meteor Crater therefore provides us with a general conceptual model

for how gully processes work, highlights the dependence of process on slope and climate, and suggests that analysis of paleodeposits and landforms alone will likely underestimate total water volume inputs, which are important considerations for understanding steep escarpments elsewhere on Earth and Mars.

#### ACKNOWLEDGMENTS

This research was supported by the National Center for Earth-surface Dynamics, the Barringer Family Fund for Meteorite Impact Research, and a Geological Society of America Graduate Student Research Grant. The light detection and ranging (LiDAR) coverage was provided by a SEED grant to the first author by the National Center for Airborne Laser Mapping (NCALM). The authors would also like to thank Ionut Iordache for his help with processing the raw LiDAR data, and the Barringer family for insightful discussions about the crater's history and permission to conduct fieldwork within the crater. Data produced from this study are available at Figshare: https://doi.org/10.6084/m9.figshare.21610215 .v2. This is Lunar and Planetary Institute (LPI) contribution No. 2883.

#### REFERENCES CITED

- Ballenger, J.A.M., Holliday, V.T., Kowler, A.L., Reitze, W.T., Prasciunas, M.M., Miller, D.S., and Windingstad, J.D., 2011, Evidence for Younger Dryas global climate oscillation and human response in the American Southwest: Quaternary International, v. 242, p. 502–519, https://doi .org/10.1016/j.quaint.2011.06.040.
- Barrows, T.T., Magee, J., Miller, G., and Fifield, L.K., 2019, The age of Wolfe Creek meteorite crater (Kandimalal), Western Australia: Meteoritics & Planetary Science, v. 54, p. 2686–2697, https://doi.org/10.1111/maps .13378.
- Berti, M., and Simoni, A., 2005, Experimental evidences and numerical modelling of debris flow initiated by channel runoff: Landslides, v. 2, p. 171–182, https://doi.org/10 .1007/s10346-005-0062-4.
- Berti, M., Genevois, R., Simoni, A., and Tecca, P.R., 1999, Field observations of a debris flow event in the Dolomites: Geomorphology, v. 29, p. 265–274, https://doi .org/10.1016/S0169-555X(99)00018-5.
- Bouwer, H., and Rice, R., 1984, Hydraulic properties of stony vadose zones: Ground Water, v. 22, p. 696–705, https://doi.org/10.1111/j.1745-6584.1984.tb01438.x.
- Bull, W.B., 1977, The alluvial-fan environment: Progress in Physical Geography, v. 1, p. 222–270, https://doi.org/10 .1177/030913337700100202.
- Bunte, K., and Abt, S.R., 2001, Sampling Surface and Subsurface Particle-Size Distributions in Wadable Graveland Cobble-Bed Streams for Analyses in Sediment Transport, Hydraulics, and Streambed Monitoring: Fort Collins, Colorado, U.S. Department of Agriculture, Forest Service, Rocky Mountain Research Station, 428 p., https://doi.org/10.2737/RMRS-GTR-74.
- Caine, T.N., 1986, Sediment movement and storage on alpine slopes in the Colorado Rocky Mountains, in Abrahams, A.B., ed., Hillslope Processes: London, Routledge, Binghamton Geomorphology Symposium 16, p. 115– 137, https://doi.org/10.4324/9781003028840.
- Cannon, S., Gartner, J., Parrett, C., and Parise, M., 2003, Wildfire-related debris-flow generation through episodic progressive sediment-bulking processes, western USA, in Chen, C.L., and Rickenmann, D., eds., Debris-Flow Hazards Mitigation: Mechanics, Prediction, and Assessment: Rotterdam, Netherlands, Millpress, p. 71–82.
- Christensen, P.R., 2003, Formation of recent Martian gullies through melting of extensive water-rich snow deposits: Nature, v. 422, p. 45–48, https://doi.org/10.1038/nature01436.

- Coe, J.A., Kinner, D.A., and Godt, J.W., 2008, Initiation conditions for debris flows generated by runoff at Chalk Cliffs, central Colorado: Geomorphology, v. 96, p. 270–297, https://doi.org/10.1016/j.geomorph.2007.03.017.
- Cole, K.L., Fisher, J.F., Ironside, K., Mead, J.I., and Koehler, P., 2013, The biogeographic histories of *Pinus edulis* and *Pinus monophylla* over the last 50,000 years: Quaternary International, v. 310, p. 96–110, https://doi.org/10.1016/j.quaint.2012.04.037.
- Coleman, K.A., Dixon, J.C., Howe, K.L., Roe, L.A., and Chevrier, V., 2009, Experimental simulation of Martian gully forms: Planetary and Space Science, v. 57, p. 711–716, https://doi.org/10.1016/j.pss.2008.11.002.
- Conway, F.M., Connor, C.B., Hill, B., Condit, C., Mullaney, K., and Hall, C., 1998, Recurrence rates of basaltic volcanism in SP cluster, San Francisco volcanic field, Arizona: Geology, v. 26, p. 655–658, https://doi.org/10.1130/0091-7613(1998)026<0655:RROBVI>2.3.CO;2.
- Conway, S.J., and Balme, M.R., 2016, A novel topographic parameterization scheme indicates that Martian gullies display the signature of liquid water: Earth and Planetary Science Letters, v. 454, p. 36–45, https://doi.org /10.1016/j.epsl.2016.08.031.
- Conway, S.J., Balme, M.R., Kreslavsky, M.A., Murray, J.B., and Towner, M.C., 2015, The comparison of topographic long profiles of gullies on Earth to gullies on Mars: A signal of water on Mars: Icarus, v. 253, p. 189–204, https://doi.org/10.1016/j.icarus.2015.03.009.
- Conway, S.J., Butcher, F.E., de Haas, T., Deijns, A.A., Grindrod, P.M., and Davis, J.M., 2018, Glacial and gully erosion on Mars: A terrestrial perspective: Geomorphology, v. 318, p. 26–57, https://doi.org/10.1016/j.geomorph.2018.05.019.
- Conway, S.J., de Haas, T., and Harrison, T.N., 2019, Martian gullies: A comprehensive review of observations, mechanisms and insights from Earth analogues, in Conway, S.J., Carrivick, J.L., Carling, P.A., de Haas, T., and Harrison, T.N., eds., Martian Gullies and their Earth Analogues: Geological Society, London, Special Publication 467, p. 7–66, https://doi.org/10.1144/SP467.14.
- Costa, J.E., 1984, Physical geomorphology of debris flows, in Costa, J.E., and Fleisher, P.J., eds., Developments and Applications of Geomorphology: Berlin, Springer, p. 268–317, https://doi.org/10.1007/978-3-642 -69759-3 9.
- Costard, F., Forget, F., Mangold, N., and Peulvast, J.P., 2002, Formation of recent Martian debris flows by melting of near-surface ground ice at high obliquity: Science, v. 295, p. 110–113, https://doi.org/10.1126/science .1066698.
- Costard, F., Forget, F., Jomelli, V., Mangold, N., and Peulvast, J.-P., 2007, Debris flows in Greenland and on Mars, in Chapman, M.G., ed., The Geology of Mars: Evidence from Earth-Based Analogs: Cambridge, UK, Cambridge University Press, Cambridge Planetary Science Volume 265, p. 265–278.
- Curry, R.R., 1966, Observation of alpine mudflows in the Tenmile Range, central Colorado: Geological Society of America Bulletin, v. 77, p. 771–776, https://doi .org/10.1130/0016-7606(1966)77[771:OOAMIT]2 .0.CO:2
- de Haas, T., Hauber, E., and Kleinhans, M.G., 2013, Local late Amazonian boulder breakdown and denudation rate on Mars: Geophysical Research Letters, v. 40, p. 3527– 3531, https://doi.org/10.1002/grl.50726.
- de Haas, T., Hauber, E., Conway, S., Van Steijn, H., Johnsson, A., and Kleinhans, M., 2015a, Earth-like aqueous debris-flow activity on Mars at high orbital obliquity in the last million years: Nature Communications, v. 6, p. 7543, https://doi.org/10.1038/ncomms8543.
- de Haas, T., Ventra, D., Hauber, E., Conway, S.J., and Kleinhans, M.G., 2015b, Sedimentological analyses of Martian gullies: The subsurface as the key to the surface: Icarus, v. 258, p. 92–108, https://doi.org/10.1016/j.icarus.2015.06.017.
- de Haas, T., McArdell, B., Conway, S., McElwaine, J., Kleinhans, M., Salese, F., and Grindrod, P., 2019, Initiation and flow conditions of contemporary flows in Martian gullies: Journal of Geophysical Research: Planets, v. 124, p. 2246–2271, https://doi.org/10.1029/2018JE005899.

1020

- Dickson, J.L., and Head, J.W., 2009, The formation and evolution of youthful gullies on Mars: Gullies as the latestage phase of Mars' most recent ice age: Icarus, v. 204, p. 63–86, https://doi.org/10.1016/j.icarus.2009.06.018.
- Dickson, J.L., Head, J.W., and Kreslavsky, M., 2007, Martian gullies in the southern mid-latitudes of Mars: Evidence for climate-controlled formation of young fluvial features based upon local and global topography: Icarus, v. 188, p. 315–323, https://doi.org/10.1016/j.icarus .2006.11.020.
- Diniega, S., Byrne, S., Bridges, N.T., Dundas, C.M., and McEwen, A.S., 2010, Seasonality of present-day Martian dune-gully activity: Geology, v. 38, p. 1047–1050, https://doi.org/10.1130/G31287.1.
- Dundas, C.M., Diniega, S., and McEwen, A.S., 2015, Long-term monitoring of Martian gully formation and evolution with MRO/HiRISE: Icarus, v. 251, p. 244–263, https://doi.org/10.1016/j.icarus.2014.05.013.
- Dundas, C.M., Conway, S.J., and Cushing, G.E., 2022, Martian gully activity and the gully sediment transport system: Icarus, v. 386, https://doi.org/10.1016/j.icarus .2022.115133.
- Dutton, C.E., 1882, Tertiary History of the Grand Cañon District, with Atlas: Washington, D.C., U.S. Government Printing Office, 446 p.
- Fairchild, H.L., 1907, Origin of meteor crater (Coon butte), Arizona: Geological Society of America Bulletin, v. 18, p. 493–504, https://doi.org/10.1130/GSAB-18-493.
- Ferguson, R., 2007, Flow resistance equations for gravel- and boulder-bed streams: Water Resources Research, v. 43, W05427, https://doi.org/10.1029/2006WR005422.
- Gallagher, C., and Balme, M., 2011, Landforms indicative of ground-ice thaw in the northern high latitudes of Mars, in Balme, M.R., Bargery, A.S., Gallagher, C.J., and Gupta, S., eds., Martian Geomorphology: Geological Society, London, Special Publication 356, p. 87–110, https://doi.org/10.1144/SP356.6.
- Gilmore, M.S., and Phillips, E.L., 2002, Role of aquicludes in formation of Martian gullies: Geology, v. 30, p. 1107–1110, https://doi.org/10.1130/0091-7613(2002)030<1107:ROAIFO>2.0.CO;2.
- Godt, J.W., and Coe, J.A., 2007, Alpine debris flows triggered by a 28 July 1999 thunderstorm in the central Front Range, Colorado: Geomorphology, v. 84, p. 80–97, https://doi.org/10.1016/j.geomorph.2006.07.009.
- Goldspiel, J.M., and Squyres, S.W., 2011, Groundwater discharge and gully formation on Martian slopes: Icarus, v. 211, p. 238–258, https://doi.org/10.1016/j.icarus.2010.10.008.
- Grant, J.A., 1999, Evaluating the evolution of process specific degradation signatures around impact craters: International Journal of Impact Engineering, v. 23, p. 331–340, https://doi.org/10.1016/S0734-743X(99)00084-6.
- Gregoretti, C., and Fontana, G.D., 2008, The triggering of debris flow due to channel-bed failure in some alpine headwater basins of the Dolomites: Analyses of critical runoff: Hydrological Processes, v. 22, p. 2248–2263, https://doi.org/10.1002/hyp.6821.
- Griffiths, P.G., Webb, R.H., and Melis, T.S., 1996, Initiation and Frequency of Debris Flows in Grand Canyon, Arizona: U.S. Geological Survey Open-File Report 96–491, 35 p., https://doi.org/10.3133/ofr96491.
- Hager, D., 1953, Crater mound (Meteor Crater), Arizona, a geologic feature: AAPG Bulletin, v. 37, no. 4, p. 821–857.
- Hales, T., and Roering, J.J., 2007, Climatic controls on frost cracking and implications for the evolution of bedrock landscapes: Journal of Geophysical Research: Earth Surface, v. 112, https://doi.org/10.1029 /2006JF000616.
- Harrison, T., Malin, M.C., and Edgett, K.S., 2009, Present-day gully activity observed by the Mars Reconnaissance Orbiter (MRO) Context Camera (CTX), in 41st Annual Meeting of the American Astronomical Society Division for Planetary Sciences Meeting, Abstracts: Fajardo, Puerto Rico, American Astronomical Society Division for Planetary Sciences, p. 57.03.
- Harrison, T.N., Osinski, G.R., Tornabene, L.L., and Jones, E., 2015, Global documentation of gullies with the Mars Reconnaissance Orbiter Context Camera and implications for their formation: Icarus, v. 252, p. 236–254, https://doi.org/10.1016/j.icarus.2015.01.022.

- Hartmann, W.K., Thorsteinsson, T., and Sigurdsson, F., 2003, Martian hillside gullies and Icelandic analogs: Icarus, v. 162, p. 259–277, https://doi.org/10.1016/S0019-1035(02)00065-9.
- Hobbs, S., Paull, D., and Clarke, J., 2013, The influence of slope morphology on gullies: Terrestrial gullies in Lake George as analogues for Mars: Planetary and Space Science, v. 81, p. 1–17, https://doi.org/10.1016/j.pss.2012 10.009.
- Howard, A.D., and McLane, C.F., 1988, Erosion of cohesionless sediment by groundwater seepage: Water Resources Research, v. 24, p. 1659–1674, https://doi.org/10.1029/WR024i010p01659.
- Huntoon, P.W., 2000, Variability of karstic permeability between unconfined and confined aquifers, Grand Canyon region, Arizona: Environmental & Engineering Geoscience, v. 6, p. 155–170, https://doi.org/10.2113/gseegeosci.6.2.155.
- Iverson, R.M., 1997, The physics of debris flows: Reviews of Geophysics, v. 35, p. 245–296, https://doi.org/10.1029/97RG00426.
- Jacobs, B.F., 1985, A middle Wisconsin pollen record from Hay Lake, Arizona: Quaternary Research, v. 24, p. 121– 130, https://doi.org/10.1016/0033-5894(85)90088-2.
- Johnson, A., and Rodine, J., 1984, Debris flow, in Brunsden, D., and Prior, D.B., eds., Slope Instability: New York, John Wiley, p. 257–361.
- Johnsson, A., Reiss, D., Hauber, E., Hiesinger, H., and Zanetti, M., 2014, Evidence for very recent melt-water and debris flow activity in gullies in a young mid-latitude crater on Mars: Icarus, v. 235, p. 37–54, https://doi.org/10.1016/j.icarus.2014.03.005.
- Kaitna, R., Palucis, M.C., Yohannes, B., Hill, K.M., and Dietrich, W.E., 2016, Effects of coarse grain size distribution and fine particle content on pore fluid pressure and shear behavior in experimental debris flows: Journal of Geophysical Research: Earth Surface, v. 121, p. 415–441, https://doi.org/10.1002/2015JF003725.
- Kean, J.W., McCoy, S.W., Tucker, G.E., Staley, D.M., and Coe, J.A., 2013, Runoff-generated debris flows: Observations and modeling of surge initiation, magnitude, and frequency: Journal of Geophysical Research: Earth Surface, v. 118, p. 2190–2207, https://doi.org/10.1002/jgrf.20148.
- Kohl, C.P., and Nishiizumi, K., 1992, Chemical isolation of quartz for measurement of in-situ-produced cosmogenic nuclides: Geochimica et Cosmochimica Acta, v. 56, no. 9, p. 3583–3587, https://doi.org/10.1016/ //0016-7037(92)90401-4.
- Kolb, K.J., Pelletier, J.D., and McEwen, A.S., 2010, Modeling the formation of bright slope deposits associated with gullies in Hale Crater, Mars: Implications for recent liquid water: Icarus, v. 205, p. 113–137, https://doi.org/10.1016/j.icarus.2009.09.009.
- Kring, D.A., 1997, Air blast produced by the Meteor Crater impact event and a reconstruction of the affected environment: Meteoritics & Planetary Science, v. 32, p. 517–530, https://doi.org/10.1111/j.1945-5100.1997.tb01297.x.
- Kring, D.A., 2007, Guidebook to the Geology of Barringer Meteorite Crater, Arizona (a.k.a. Meteor Crater): Houston, Texas, Lunar and Planetary Institute, 150 p., http://www.lpi.usra.edu/publications/books/barringer \_crater\_guidebook/ (accessed March 2016).
- Kring, D.A., 2017, Guidebook to the Geology of Barringer Meteorite Crater, Arizona (a.k.a. Meteor Crater) (second edition): Lunar and Planetary Institute Contribution 2040, 272 p.
- Kumar, P.S., and Kring, D.A., 2008, Impact fracturing and structural modification of sedimentary rocks at Meteor Crater, Arizona: Journal of Geophysical Research: Planets, v. 113, https://doi.org/10.1029 /20081F003115
- Kumar, P.S., Head, J.W., and Kring, D.A., 2010, Erosional modification and gully formation at Meteor Crater, Arizona: Insights into crater degradation processes on Mars: Icarus, v. 208, p. 608–620, https://doi.org/10 .1016/j.icarus.2010.03.032.
- Lal, D., and Peters, B., 1967, Cosmic ray produced radioactivity on the Earth, in Sitte, K., ed., Kosmische Strahlung II (Cosmic Rays II): Berlin, Springer, Handbuch der Physik (Encyclopedia of Physics), p. 551–612, https://doi.org/10.1007/978-3-642-46079-1\_7.

- Lamb, M.P., Howard, A.D., Johnson, J., Whipple, K.X., Dietrich, W.E., and Perron, J.T., 2006, Can springs cut canyons into rock?: Journal of Geophysical Research: Planets, v. 111, https://doi.org/10.1029/2005JE002663.
- Lamb, M.P., Scheingross, J.S., Amidon, W.H., Swanson, E., and Limaye, A., 2011, A model for fire-induced sediment yield by dry ravel in steep landscapes: Journal of Geophysical Research: Earth Surface, v. 116, https://doi .org/10.1029/2010JF001878.
- Laskar, J., Correia, A.C.M., Gastineau, M., Joutel, F., Levrard, B., and Robutel, P., 2004, Long term evolution and chaotic diffusion of the insolation quantities of Mars: Icarus, v. 170, p. 343–364, https://doi.org/10.1016/j.icarus.2004.04.005.
- Levy, J.S., Head, J.W., Dickson, J.L., Fassett, C.I., Morgan, G.A., and Schon, S.C., 2010, Identification of gully debris flow deposits in Protonilus Mensae, Mars: Characterization of a water-bearing, energetic gully-forming process: Earth and Planetary Science Letters, v. 294, p. 368–377, https://doi.org/10.1016/j.epsl.2009.08.002.
- Major, J.J., and Pierson, T.C., 1992, Debris flow rheology: Experimental analysis of fine-grained slurries: Water Resources Research, v. 28, p. 841–857, https://doi.org/10.1029/91WR02834.
- Malin, M.C., and Edgett, K.S., 2000, Evidence for recent groundwater seepage and surface runoff on Mars: Science, v. 288, p. 2330–2335, https://doi.org/10.1126/science.288.5475.2330.
- Malin, M.C., Edgett, K.S., Posiolova, L.V., McColley, S.M., and Dobrea, E.Z.N., 2006, Present-day impact cratering rate and contemporary gully activity on Mars: Science, v. 314, p. 1573–1577, https://doi.org/10.1126/science .1135156.
- Mangold, N., Mangeney, A., Migeon, V., Ansan, V., Lucas, A., Baratoux, D., and Bouchut, F., 2010, Sinuous gullies on Mars: Frequency, distribution, and implications for flow properties: Journal of Geophysical Research: Planets, v. 115, https://doi.org/10.1029/2009JE003540.
- Mangold, N., Kite, E., Kleinhans, M., Newsom, H., Ansan, V., Hauber, E., Kraal, E., Quantin, C., and Tanaka, K., 2012, The origin and timing of fluvial activity at Eberswalde crater, Mars: Icarus, v. 220, p. 530–551, https:// doi.org/10.1016/j.icarus.2012.05.026.
- Marrero, S., Phillips, F.M., Caffee, M.W., Smith, S.S., and Kring, D.A., 2010, Re-dating the Barringer meteorite crater (AZ) impact using the cosmogenic chlorine-36 surface exposure method: Meteoritics & Planetary Science, v. 73, Supplement, p. 5150, https://www.lpi.usra .edu/meetings/metsoc2010/pdf/5150.pdf.
- Matsubara, Y., and Howard, A.D., 2009, A spatially explicit model of runoff, evaporation, and lake extent: Application to modern and late Pleistocene lakes in the Great Basin region, western United States: Water Resources Research, v. 45, https://doi.org/10.1029/2007WR005953.
- McCoy, S.W., Kean, J.W., Coe, J.A., Staley, D.M., Wasklewicz, T.A., and Tucker, G.E., 2010, Evolution of a natural debris flow: In situ measurements of flow dynamics, video imagery, and terrestrial laser scanning: Geology, v. 38, p. 735–738, https://doi.org/10.1130/G30928.1.
- McKee, E.D., 1947, Experiments on the development of tracks in fine cross-bedded sand: Journal of Sedimentary Research, v. 17, no. 1, p. 23–28, https://doi.org/10 .1306/D4269292-2B26-11D7-8648000102C1865D.
- Mellon, M.T., and Phillips, R.J., 2001, Recent gullies on Mars and the source of liquid water: Journal of Geophysical Research: Planets, v. 106, p. 23,165–23,179, https://doi.org/10.1029/2000JE001424.
- Merrill, G.P., 1908, The meteor crater of Canyon Diablo, Arizona: Its history, origin, and associated meteoritic irons: Smithsonian Miscellaneous Collections, v. 50, p. 461–498.
- Meyer, G.A., and Well, S.G., 1997, Fire-related sedimentation events on alluvial fans, Yellowstone National Park, U.S.A.: Journal of Sedimentary Research, v. 67, no. 5, p. 776–791, https://doi.org/10.1306/D426863A-2B26-11D7-8648000102C1865D.
- Morgan, A.M., Howard, A.D., Hobley, D.E.J., Moore, J.M., Dietrich, W.E., Williams, R.M.E., Burr, D.M., Grant, J.A., Wilson, S.A., and Matsubara, Y., 2014, Sedimentology and climatic environment of alluvial fans in the Martian Saheki Crater and a comparison with terrestrial

- fans in the Atacama Desert: Icarus, v. 229, p. 131–156, https://doi.org/10.1016/j.icarus.2013.11.007.
- Mustard, J.F., Cooper, C.D., and Rifkin, M.K., 2001, Evidence for recent climate change on Mars from the identification of youthful near-surface ground ice: Nature, v. 412, p. 411–414, https://doi.org/10.1038/35086515.
- Nagata, N., Hosoda, T., and Muramoto, Y., 2000, Numerical analysis of river channel processes with bank erosion: Journal of Hydraulic Engineering, v. 126, p. 243–252, https://doi.org/10.1061/(ASCE)0733-9429(2000)126:4(243).
- National Oceanic and Atmospheric Administration (NOAA), 2011, Precipitation-Frequency Atlas of the United States: NOAA Atlas 14, Volume 1, Version 5, https:// www.weather.gov/media/owp/oh/hdsc/docs/Atlas14\_ Volume1.pdf.
- Nishiizumi, K., Winterer, E., Kohl, C., Klein, J., Middleton, R., Lal, D., and Arnold, J., 1989, Cosmic ray production rates of <sup>10</sup>Be and <sup>26</sup>Al in quartz from glacially polished rocks: Journal of Geophysical Research: Solid Earth, v. 94, p. 17,907–17,915, https://doi.org/10.1029/JB094iB12p17907.
- Nishiizumi, K., Kohl, C.P., Shoemaker, E.M., Arnold, J.R., Klein, J., Fink, D., and Middleton, R., 1991, In situ <sup>10</sup>Be-<sup>26</sup>Al exposure ages at Meteor Crater, Arizona: Geochimica et Cosmochimica Acta, v. 55, p. 2699–2703, https://doi.org/10.1016/0016-7037(91)90388-L.
- Núñez, J., Barnouin, O., Murchie, S., Seelos, F., McGovern, J., Seelos, K., and Buczkowski, D., 2016, New insights into gully formation on Mars: Constraints from composition as seen by MRO/CRISM: Geophysical Research Letters, v. 43, p. 8893–8902, https://doi.org/10.1002 /2016GL068956.
- Palucis, M.C., Dietrich, W.E., Hayes, A.G., Williams, R.M.E., Gupta, S., Mangold, N., Newsom, H., Hardgrove, C., Calef, F., and Sumner, D.Y., 2014, The origin and evolution of the Peace Vallis fan system that drains to the Curiosity landing area, Gale Crater, Mars: Journal of Geophysical Research: Planets, v. 119, p. 705–728, https://doi.org/10.1002/2013JE004583.
- Palucis, M.C., Morgan, A.M., Strauss, J.V., Rivera-Hernandez, F., Marshall, J.A., Menio, E., and Miller, R., 2023, Rates and processes controlling periglacial alluvial fan formation: Implications for Martian fans: Geological Society of America Bulletin, v. 135, p. 937–954, https://doi.org/10.1130/B36459.1.
- Parsons, R.A., and Nimmo, F., 2010, Numerical modeling of Martian gully sediment transport: Testing the fluvial hypothesis: Journal of Geophysical Research: Planets, v. 115, https://doi.org/10.1029/2009JE003517.
- Pasquon, K., Gargani, J., Massé, M., and Conway, S.J., 2016, Present-day formation and seasonal evolution of linear dune gullies on Mars: Icarus, v. 274, p. 195–210, https://doi.org/10.1016/j.icarus.2016.03.024.
- Pepin, E., Carretier, S., and Herail, G., 2010, Erosion dynamics modelling in a coupled catchment-fan system with constant external forcing: Geomorphology, v. 122, p. 78–90, https://doi.org/10.1016/j.geomorph.2010.04.029.
- Phillips, F.M., Zreda, M.G., Smith, S.S., Elmore, D., Kubik, P.W., Dorn, R.I., and Roddy, D.J., 1991, Age and geomorphic history of Meteor Crater, Arizona, from cosmogenic <sup>36</sup>Cl and <sup>14</sup>C in rock varnish: Geochimica et Cosmochimica Acta, v. 55, p. 2695–2698, https://doi.org/10.1016/0016-7037(91)90387-K.
- Pierson, T.C., 1981, Dominant particle support mechanisms in debris flows at Mt. Thomas, New Zealand, and implicacions for flow mobility: Sedimentology, v. 28, p. 49–60, https://doi.org/10.1111/j.1365-3091.1981.tb01662.x.
- Pilon, J.A., Grieve, R.F., and Sharpton, V.L., 1991, The subsurface character of Meteor Crater, Arizona, as determined by ground-probing radar: Journal of Geophysical Research: Planets, v. 96, p. 15,563–15,576, https://doi.org/10.1029/91JE01114.
- Piqueux, S., Kleinböhl, A., Hayne, P.O., Kass, D.M., Schofield, J.T., and McCleese, D.J., 2015, Variability of the Martian seasonal CO<sub>2</sub> cap extent over eight Mars years: Icarus, v. 251, p. 164–180, https://doi.org/10 .1016/j.icarus.2014.10.045.
- Prancevic, J.P., Lamb, M.P., and Fuller, B.M., 2014, Incipient sediment motion across the river to debris-flow transition: Geology, v. 42, p. 191–194, https://doi.org/10 .1130/G34927.1.

- Raack, J., Reiss, D., Appéré, T., Vincendon, M., Ruesch, O., and Hiesinger, H., 2015, Present-day seasonal gully activity in a south polar pit (Sisyphi Cavi) on Mars: Icarus, v. 251, p. 226–243, https://doi.org/10.1016/j.icarus.2014.03.040.
- Reger, R.D., and Batchelder, G.L., 1971, Late Pleistocene molluscs and a minimum age of Meteor Crater, Arizona: Journal of the Arizona Academy of Science, v. 6, p. 190–195, https://doi.org/10.2307/40025639.
- Rinehart, J.S., 1958, On the nature of the meteoritic debris at the Arizona Meteorite Crater: The Astronomical Journal, v. 63, p. 310, https://doi.org/10.1086/107761.
- Roddy, D.J., 1978, Pre-Impact Geologic Conditions, Physical Properties, Energy Calculations, Meteorite and Initial Crater Dimensions and Orientations of Joints, Faults and Walls at Meteor Crater, Arizona: Lunar and Planetary Science Conference Proceedings, http://ntrs.nasa.gov/search.jsp?R=19790055303 (accessed March 2016).
- Schneider, J.M., Rickenmann, D., Turowski, J.M., Bunte, K., and Kirchner, J.W., 2015, Applicability of bed load transport models for mixed-size sediments in steep streams considering macro-roughness: Water Resources Research, v. 51, p. 5260–5283, https://doi.org/10 .1002/2014WR016417.
- Schon, S., and Head, J., 2009, Terraced cutbanks and longitudinal bars in gully channels on Mars: Evidence for multiple episodes of fluvial transport: 40th Lunar and Planetary Science Conference, abstract 1691, https://www.lpi.usra.edu/meetings/lpsc2009/pdf /1691.pdf.
- Schumm, S.A., Boyd, K.F., Wolff, C.G., and Spitz, W.J., 1995, A ground-water sapping landscape in the Florida Panhandle: Geomorphology, v. 12, p. 281–297, https:// doi.org/10.1016/0169-555X(95)00011-S.
- Shoemaker, E.M., 1959, Impact Mechanics at Meteor Crater, Arizona: U.S. Geological Survey Open-File Report 59-108, 55 p., https://doi.org/10.3133/ofr59108.
- Shoemaker, É.M., 1960, Penetration mechanics of high velocity meteorites: Illustrated by Meteor Crater, Arizona, in McCall, G.J.H., ed., 21st International Geological Congress: Copenhagen, Denmark, International Geological Congress Proceedings, p. 418–434.
- Shoemaker, E.M., 1987, Rocky Mountain Section of the Geological Society of America: Boulder, Colorado, Geological Society of America, Decade of North American Geology, Centennial Field Guide Volume 2, 483 p., https://doi.org/10.1130/0-8137-5402-X.
- Shoemaker, E.M., and Kieffer, S.W., 1974, Guidebook to the geology of Meteor Crater, Arizona, in 37th Annual Meeting of the Meteoritical Society: Tempe, Arizona, Center for Meteorite Studies, Arizona State University, 66 p.
- Shoemaker, E.M., and Kieffer, S.W., 1979, Guidebook to the Geology of Meteor Crater, Arizona: Tempe, Arizona, Center for Meteorite Studies, Arizona State University, Publication 17, 71 p.
- Sinha, R.K., Vijayan, S., Shukla, A.D., Das, P., and Bhattacharya, F., 2019, Gullies and debris-flows in Ladakh Himalaya, India: A potential Martian analogue, in Conway, S.J., Carrivick, J.L., Carling, P.A., de Haas, T., and Harrison, T.N., eds., Martian Gullies and their Earth Analogues: Geological Society, London, Special Publication 467, p. 315–342, https://doi.org/10.1144/SP467.9.
- Staley, D.M., Kean, J.W., and Rengers, F.K., 2020, The recurrence interval of post-fire debris-flow generating rainfall in the southwestern United States: Geomorphology, v. 370, https://doi.org/10.1016/j.geomorph.2020.107392.
- Sutton, S.R., 1985, Thermoluminescence measurements on shock-metamorphosed sandstone and dolomite from Meteor Crater, Arizona: 2. Thermoluminescence age of meteor crater: Journal of Geophysical Research: Solid Earth, v. 90, p. 3690–3700, https://doi.org/10.1029/JB090iB05p03690.
- Takahashi, T., 1978, Mechanical characteristics of debris flow: Journal of the Hydraulics Division, v. 104, p. 1153–1169, https://doi.org/10.1061/JYCEAJ.0005046.
- Vincendon, M., Forget, F., and Mustard, J., 2010a, Water ice at low to midlatitudes on Mars: Journal of Geophysical Research: Planets, v. 115, https://doi.org/10.1029 /2010JE003584.

- Vincendon, M., Mustard, J., Forget, F., Kreslavsky, M., Spiga, A., Murchie, S., and Bibring, J.-P., 2010b, Near-tropical subsurface ice on Mars: Geophysical Research Letters, v. 37, L01202, https://doi.org/10.1029/2009GL041426.
- Wagner, J.D.M., Cole, J.E., Beck, J.W., Patchett, P.J., Henderson, G.M., and Barnett, H.R., 2010, Moisture variability in the southwestern United States linked to abrupt glacial climate change: Nature Geoscience, v. 3, p. 110–113, https://doi.org/10.1038/ngeo707.Warner, N.H., Gupta, S., Kim, J.-R., Muller, J.-P., Le Corre,
- Warner, N.H., Gupta, S., Kim, J.-R., Muller, J.-P., Le Corre, L., Morley, J., Lin, S.-Y., and McGonigle, C., 2011, Constraints on the origin and evolution of Iani Chaos, Mars: Journal of Geophysical Research: Planets, v. 116, https://doi.org/10.1029/2010JE003787.
- Whipple, K.X., and Dunne, T., 1992, The influence of debris-flow rheology on fan morphology, Owens Valley, California: Geological Society of America Bulletin, v. 104, p. 887–900, https://doi.org/10 .1130/0016-7606(1992)104<0887:TIODFR> 2.3.CO;2.
- Wolman, M.G., 1954, A method of sampling coarse river-bed material: Eos, v. 35, p. 951–956, https://doi.org/10.1029 /TR035i006p00951.
- Zhu, C., and Kipfer, R., 2010, Noble gas signatures of high recharge pulses and migrating jet stream in the late Pleistocene over Black Mesa, Arizona, United States: Geology, v. 38, p. 83–86, https://doi.org/10.1130 //G30369.1.
- Zhu, C., Waddell, R.K., Star, I., and Ostrander, M., 1998, Responses of ground water in the Black Mesa basin, northeastern Arizona, to paleoclimatic changes during the late Pleistocene and Holocene: Geology, v. 26, p. 127–130, https://doi.org/10.1130 //0091-7613(1998)026<0127:ROGWIT>2.3.CO;2.

SCIENCE EDITOR: MIHAI DUCEA ASSOCIATE EDITOR: EMMANUEL GABET

MANUSCRIPT RECEIVED 23 NOVEMBER 2022 REVISED MANUSCRIPT RECEIVED 2 FEBRUARY 2023 MANUSCRIPT ACCEPTED 29 MARCH 2023

Printed in the USA